2016

Thermoelectric Transport and Energy Conversion Using Novel 2D Materials

Luke J. Wirth
Wright State University

THERMOELECTRIC TRANSPORT AND ENERGY CONVERSION USING NOVEL 2D MATERIALS

A thesis submitted in partial fulfillment of the requirements for the degree of Master of Science in Renewable and Clean Energy Engineering

By

LUKE J. WIRTH
B.S., Stanford University, 2014

2016
Wright State University

WRIGHT STATE UNIVERSITY

GRADUATE SCHOOL

Dec 19, 2016

I HEREBY RECOMMEND THAT THE THESIS PREPARED UNDER MY SUPERVISION BY Luke J. Wirth ENTITLED THERMOELECTRIC TRANSPORT AND ENERGY CONVERSION USING NOVEL 2D MATERIALS BE ACCEPTED IN PARTIAL FULFILLMENT OF THE REQUIREMENTS FOR THE DEGREE OF Master of Science in Renewable and Clean Energy Engineering.

Amir A. Farajian, Ph.D.
Thesis Director

Committee on Final Examination

Joseph C. Slater, Ph.D., P.E.
Chair, Department of Mechanical
and Materials Engineering

Amir A. Farajian, Ph.D.

Hong Huang, Ph.D.

James A. Menart, Ph.D.

Robert E. W. Fyffe, Ph.D.
Vice President for Research and
Dean of the Graduate School

ABSTRACT

Wirth, Luke J. M.S.R.C.E.E. Department of Mechanical and Materials Engineering, Wright State University, 2016. THERMOELECTRIC TRANSPORT AND ENERGY CONVERSION USING NOVEL 2D MATERIALS.

Nanomaterials hold great promise for applications in thermal management and thermoelectric power generation. Defects in these are important as they are generally inevitably introduced during fabrication or intentionally engineered to control the properties of the nanomaterials. Here, we investigate how phonon-contributed thermal conductance in narrow graphene, boron nitride (BN), and silicene nanoribbons (NRs), responds to the presence of a vacancy defect and the corresponding geometric distortion, from first principles using the non-equilibrium Green's function method. Analyses are made of the geometries, phonon conductance coefficients, and local densities of states (LDOS) of pristine and defected nanoribbons. It is found that hydrogen absences produce similar reductions in thermal conductance in planar graphene and BN NRs with greater reductions in buckled silicene NRs. Vacancies of larger atoms affect all systems similarly, causing greater reductions than hydrogen absences. Emerging flexible and stiff scattering centers, depending on bond strengths, are shown to cause thermal conductance reduction by changing nearby LDOSs in defected structures relative to pristine ones. This knowledge suggests that inferences on unknown thermal properties of novel defected materials can be made based on understanding how thermal transport behaves in their analogues and how bond characteristics differ between systems under consideration.

The thermal conductance contributed by phonons is often a limiting factor to the overall suitability of a material for use in thermoelectric power generation, wherein a voltage is generated in a material by a temperature gradient. The thermoelectric figure of merit (ZT) assesses this suitability, in part based on a ratio of electrical conductance to thermal conductance. These two properties can be decoupled in low-dimensional structures like NRs, with lower thermal conductances generally found in narrower materials. Here, ZT is analyzed in graphene, BN, and silicene nanoribbons of two different widths with engineered edges that are designed to increase the ratio of edge length to NR length. This could conceivably be synthesized by either top-down or bottom-up methods. Analyses are made of how width and material change the maximum ZT attainable by controlling the chemical potential of each system, how these maximum ZTs differ in each system as a result of p- or n- type change to chemical potential, how full-width half-maximum values of ZT peaks behave, and how the different factors of ZT affect its final value in these systems. A very high ZT of 6.26 is reported near the bandgap in the narrow chevron silicene NR at room temperature, and a room temperature ZT greater than 3 is also found in the narrow BN NR, suggesting that edge-engineered NRs offer high promise for thermoelectric applications and may be suitable for emissions-free electricity generation from waste heat sources.

TABLE OF CONTENTS

Page

LIST OF FIGURES

Figure Page

LIST OF TABLES

Table Page

PREFACE

This thesis is primarily based on two manuscripts.

The first of these was published in *Applied Physics Letters* **109**, 173102 (2016) as "Resilience of thermal conductance in defected graphene, silicene, and boron nitride nanoribbons" by Luke J. Wirth, Tim H. Osborn, and Amir A. Farajian.

The second, "Systematic enhancement of thermoelectric figure of merit in edge-engineered nanoribbons" by Luke J. Wirth and Amir A. Farajian, is under review at the time of thesis submission.

ACKNOWLEDGEMENTS

I would like to express my sincere gratitude to my advisor, Amir A. Farajian, for introducing me to the exciting field of computational materials science. Dr. Farajian's continual guidance, encouragement, and support made the process of preparing this thesis a thoroughly engaging, interesting, and insightful one.

I would also like to thank Dr. Olga V. Pupysheva for thoughtful comments concerning the chemistry of the systems considered here.

And, I am thankful for resources provided by the Ohio Supercomputer Center, which were essential to producing these results.

I. INTRODUCTION

Nanomaterials are currently receiving immense scientific attention for their unique physical properties, many of which offer promise for solving contemporary, global issues in science and engineering. New materials are continually emerging and production methods are becoming increasingly refined, allowing for more experiments on their properties to be conducted. The field of computational materials science allows for simulations of these properties to supplement experimental results, or even more helpfully, to make accurate predictions of how nanomaterials may behave when an experiment is impractical, e.g. to study several nanoribbons that have not been but could be synthesized, in order to assess their promise for future applications.

In this thesis, some of these properties and the principles behind computational materials science are discussed in greater depth, before analyses are performed on the thermal conductance and thermoelectric figures of merit of various graphene, boron nitride, and silicene nanoribbons. Thermal conductance is a limiting factor on this figure of merit, which assesses the suitability of a material to convert thermal energy into electricity. Materials with high figures of merit are excellent candidates for deployment in thermoelectric power generators, which offer promise as emissions-free sources of electricity, capable of being powered by waste heat as opposed to hydrocarbon fuels.

II. BACKGROUND

THERMAL CONDUCTIVITY OF NANOMATERIALS

Thermal management and thermoelectric power generation at the nanoscale are becoming increasingly possible due to novel materials, processing methods, and manipulation techniques. Successful applications of both of these will depend heavily on the thermal conductance of materials being used. This conductance can change dramatically when defects are present, as is a common occurrence during synthesis and/or when introduced intentionally via innovative means. [1–4]. Pristine nanomaterials may seem like strong candidates for thermal management purposes, but a detailed understanding of how thermal conductance will change when defects do occur is necessary to establish accurate and realistic expectations for future applications. Knowledge of this behavior will precede forthcoming solucctions to pressing problems in science and engineering, especially when deployed in conjunction with their generally more commonly studied electronic properties [5].

One of the most well-known nanomaterials, graphene, appears to be exceptionally well-suited for thermal management with a thermal conductivity of 3000-5000 W/m·K at room temperature [6,7]; this is an order of magnitude higher than that of the conventionally good conductor copper (400 W/m·K) [8,9]. Some particular applications may be in nanocircuits and Li-ion batteries, where ineffective heat dissipation often causes failure [7, 10–12]. Defects, however, will be a major obstacle to this sort of application. A recent molecular dynamics (MD) study reports that defects could reduce conductivity in graphene by two orders of magnitude, eliminating its suitability for either of the mentioned purposes [13].

On the other hand, these defects may actually enhance graphene's suitability in thermoelectric devices. Some of its analogues, like boron nitride (BN) and silicene are also generating interest because of their own unique properties, among them relatively smaller thermal conductivities. MD simulations project that thermal conductivity is 278 and 588 W/m·K in infinitely long armchair and

zigzag-edged BN nanoribbons, respectively, as well as 60–65 W/m·K and 65–70 W/m·K in zigzag and armchair-edged silicene nanoribbons (NRs) with a width of ∼5nm and lengths between ∼ 30 and ∼ 50 nm [14, 15]. NRs made of these two materials offer promise for converting temperature gradients to voltages via the thermoelectric effect, which is more efficient in materials with low thermal conductances [16–18]. Defects, such as edge roughness [19–21], could further enhance this suitability of NRs made out of any of these three materials, or others.

THE THERMOELECTRIC EFFECT IN NANOMATERIALS

Thermoelectric power generation occurs when a voltage is produced in the presence of a thermal gradient because of the process known as the Seebeck effect, with its efficiency described by the figure of merit

$$ZT = \frac{\sigma S^2 T}{(\kappa_e + \kappa_p)}, \tag{1}$$

where σ is electrical conductance, S is the Seebeck coefficient or thermopower, κ_e is the electron-contributed thermal conductance, and κ_p is the phonon-contributed thermal conductance.

Traditionally, thermoelectric devices have not been widespread because of their high costs and low efficiencies, aside from niche applications like spacecraft where these considerations are of low concern [22]. The primary obstacle to increasing their efficiency has been the interdependence of electrical and thermal conductance [23]. Achieving a figure of merit over 3 is the general goal for thermoelectric materials to be competitive with mechanical power generation in terms of efficiency [24]. For sake of making a comparison, bulk bismuth telluride thermoelectric refrigeration devices, which are available on the consumer market, have a maximum ZT of 1.2 after being optimized by nanostructuring [25]. Nanomaterials offer unique promise for thermoelectric power generation relative to bulk materials, because their low-dimensional structures can confine phonons to suppress thermal transport while still allowing electronic transport, resulting in high ZTs [26, 27].

These can be achieved even at room temperature, which further enhances the appeal of nanomaterials for thermoelectric power generation [28]. Knowledge of which of these materials hold especially high figures of merit will precede their roles in solutions to global problems like energy generation and emissions reduction.

Nanoribbons in particular have been a frequent target of thermoelectric research because manipulation of their phonon effects can lower their thermal conductance, a factor that limits ZT [29, 30]. Assessments of graphene are common, and its analogues boron nitride (BN) and silicene have also been studied due to their lower thermal conductances [6,7,14,15]. These lower conductances emerge through greater scattering; silicene has particularly low conductances due to its buckled rather than perfectly planar structure, which strongly scatters its acoustic out-of-plane phonon modes relative to graphene [31,32]. Computations concerning many varied types of NRs have found ZTs at or above unity at room temperature in graphene NRs [33–38, 38–40], BN NRs [41], graphene-BN heterostructured NRs [42, 43], silicene NRs [18, 44, 45], and in other similar one-dimensional materials like carbon nanotubes [46] and nanowires [47]. One study in particular, using a quantum model, found ZT of 2.7 in a chevron-patterned[1] graphene nanoribbon modified by isotope distribution [38]. The structure was synthesized in 2010 utilizing a bottom-up approach using etraphenyl-triphenylene monomers as precursors on an Au(111) substrate [48]. The electronic properties of several other variations of chevron nanoribbons were studied including changes in corner angle [49] and corner-corner length [50], as well as the application of an external electric field [51]. A thermoelectric properties study has been done when armchair-edge to zigzag-edge ratio varies [52].

In this report, the ab initio-based non-equilibrium Green's function (NEGF) method is used to analyze how thermoelectric properties change in chevron nanoribbons (CNRs) as material and width vary. CNRs were chosen due to their edge-

[1] A chevron structure is basically a large zig-zag pattern; this pattern is unrelated to the zig-zag edges of nanoribbons that are commonly studied in the literature. "Chevron" appears to be the closest thing to a conventional name for this shape, but other names are sometimes used like "jagged" and "nanowiggle."

engineered geometry that results in reduction of phonon transport because of their high edge to surface area ratio. It is known that phonon-boundary scattering is a limiting factor for phonon-contributed thermal conductance in narrow systems [30]. Here, graphene CNRs are considered along with BN and silicene ones, which were chosen for their low thermal conductances as previously mentioned. Two widths $\lesssim 1$ nm are chosen based on the observation that thermal conductance increases with increasing width in pseudo-one-dimensional graphene nanoribbons [53, 54]. Production of such nanoribbons may be possible using a bottom-up method similar to that which produced the CNRs mentioned above but with smaller precursors [48], or by taking a top-down approach like using OH radicals as "chemical scissors," which are capable of cutting graphene sheets grown on arbitrary substrates into any shape [55]. This method could also be applied to BN sheets grown on Ni [56] or silicene sheets grown on Ag [57]. The results presented here show systematic improvement of the thermoelectric figure of merit in edge-engineered CNRs, beyond the efficiency figure necessary to compete with mechanical power generation.

AB INITIO METHODS AND COMPUTATIONAL MATERIALS SCIENCE CONCEPTS

One of the most well-known and important equations in quantum mechanics is Schrödinger's equation, which describes the quantum state of a system in a way that Newton's second law ($F = ma$) describes the classical state of a system, and was first published in 1926 [58]. In its simplest, general, time-independent form, it is written:

$$\hat{H}\Psi = E\Psi \tag{2}$$

where $\hat{H}$ is the Hamiltonian operator, which is the sum of the system's kinetic and potential energy operators, Ψ is the system's wave function, which is a probability amplitude and in this specific case a stationary state, and E is the energy of that

state.

Solving this equation is valuable because once the energy of a system is determined, other physical and chemical properties can be calculated. However, solving it is a very non-trivial task, and many approaches have been developed for this purpose.

One iterative approach developed just after Schrödinger's equation was published is known as the Hartree-Fock (HF) method. In extremely simple terms, its basic premise is that the wavefunction of a system can be approximated by the determinant of an antisymmetric matrix of orbital products. An advantage of this method is that it allows for an *ab initio* approach to be taken, which means that calculations are performed based only on fundamental physical concepts rather than the generation of estimates based on empirically-derived quantities from different systems. [2] Despite the early emergence of HF theory, it would not be widely practically applicable until computers were capable of carrying out the necessary calculations. Once that capability did become available, HF would remain the most widely used ab initio method into the mid-2000s[3] [59].

Another development crucial to the field of computational materials science (CMS) was that of density functional theory (DFT), introduced to the world in a pair of papers by Hohenberg & Kohn in 1964 [60] and Kohn & Sham in 1965 [61]. (Kohn would go on to win the Nobel Prize in Chemistry in 1998 for his contributions [62].) In this approach, the density of electrons within a system (often referred to as an *electron gas*) are used to calculate the energy of a system, which once again is used to calculate other chemical and physical properties. The HF method can be applied within DFT calculations, so it should come as no surprise that DFT calculations similarly did not become commonplace until computers were sufficiently developed to handle such resource-intensive calculations.

Further improvements to HF and DFT were developed over the years, and

[2]While HF is a method, it is important to understand that the calculations performed by using any method are guided by a *basis set*. Basis sets are combinations of functions used to construct orbitals. Different methods can be combined with different basis sets as desired.

[3]The use of "2000s" here refers to the decade.

have been deployed increasingly frequently in the last decade. A "standard" contemporary method applied in DFT calculations is B3LYP, named for the scientists Becke, Lee, Yang, and Parr who developed it, and the 3-parameter approach that it takes to calculate the electron exchange correlational (which, simply put, is a quantum mechanical effect occurring between like particles). This particular method applies elements of both HF theory and DFT to make more accurate approximations [63–65]. Its status as a standard can be easily verified by looking at a list of the 100 most frequently cited papers of all time that *Nature* put together in 2014 [66]; the works by Hohenberg-Kahn [60] and Kohn-Sham [61] are 20th and 21st, and are immediately followed by those by Becke [65] and Lee, Yang, and Parr [64] at 22nd and 23rd.

It is worth noting that CMS makes a fully quantum analysis of the systems considered here possible, which is necessary to fully account for the effects that govern their electronic and thermal transport properties. There are effectively four tiers of transport theory: classical, which treats system elements like electrons as "hard spheres"; Boltzmann transport, which accounts for the response of a system when exposed to non-equilibrium conditions; semi-classical, which restricts the behavior of particles in the Boltzmann model to have energies within a defined band structure[4]; and quantum, which accounts for particle tunneling through classically forbidden regions, quantum conductance, and spin-mediated effects [67]. A quantum approach is particularly important for the following systems because these effects do have a significant impact on the properties of low-dimensional structures [68].

[4]Band structures are commonly plotted for both electrons and phonons; the former as energy as a function of $\vec{k}$, a vector in k-space, and the latter as frequency as a function of $\vec{k}$.

III. METHODOLOGY

EVALUATING PHONON-CONTRIBUTED THERMAL CONDUCTANCE

Before ab initio-based quantum transport calculations were performed to determine the thermal conductances and thermoelectric figures of merit of the various graphene, BN, and silicene nanoribbon systems, all of them were optimized, taking into account ground state spin multiplicities, via a density functional theory (DFT) analysis using the Becke, 3-parameter, Lee-Yang-Parr (B3LYP) method and 6–31G(d) basis set within the Gaussian 09 suite [63, 64, 69]. Gaussian uses a gradient-based optimization approach, using its Berny algorithm to reconfigure the system in a manner that minimizes its energy [70]. The aim of this and other CMS programs is to determine a geometrical configuration near system's ground state structure (or that of a saddle point, desirable in specific circumstances). The means of calculating the system's energy at each step and the accuracy of the final results depend upon the input parameters, method, and basis set used.

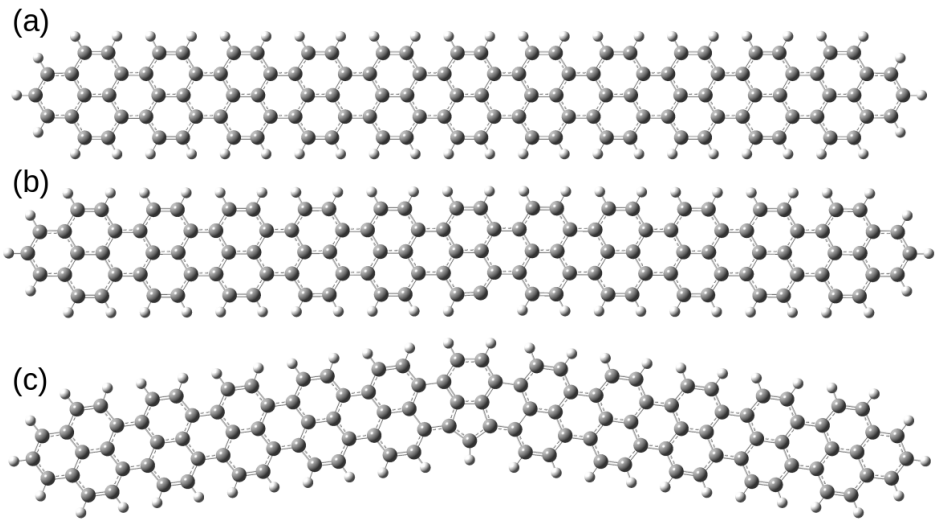

Figure 1: Optimized segments of hydrogen-passivated graphene nanoribbons in (a) the pristine case, (b) with a defect created by removing a single hydrogen atom, (c) with a defect created by removing a single carbon atom and the hydrogen that was attached to it. Following optimization, junction, left, and right contact nanoribbon segments were extracted for semi-infinite quantum transport calculations.

The resilience of thermal conductance in the presence of a single edge vacancy defect was explored by first constructing five-atom wide, hydrogen-passivated

nanoribbons made out of each material, with armchair edges, which are more stable than zigzag edges in graphene [71]. Hydrogen absences were analyzed in all nanoribbons, as well as carbon in graphene, both boron and nitrogen in BN, and silicon in silicene, making for 11 different systems. Structural configurations of systems containing 166 atoms (pristine), 165 atoms (H defect), and 164 atoms (X defect) were chosen for optimization. Figure 1 displays these for graphene, and BN and silicene segments can be found in the appendix on pages 35 and 36. These nanoribbons represent "segments" of infinite nanoribbons that are made up of 14-atom unit cells. In these segments, the three central unit cells (including the defect if one is present) act as a junction region that connects left and right contact ribbons. These contact ribbons are represented by two unit cells each, to the left and right of the junction; their geometries are repeated periodically and infinitely in the next stage of analysis. The atoms beyond these portions in these optimized segments are not considered beyond this stage; their inclusion during optimization is necessary to avoid the presence of open boundary effects in the extracted left and right contact segments. Optimized junction structures are shown in Figure 2.

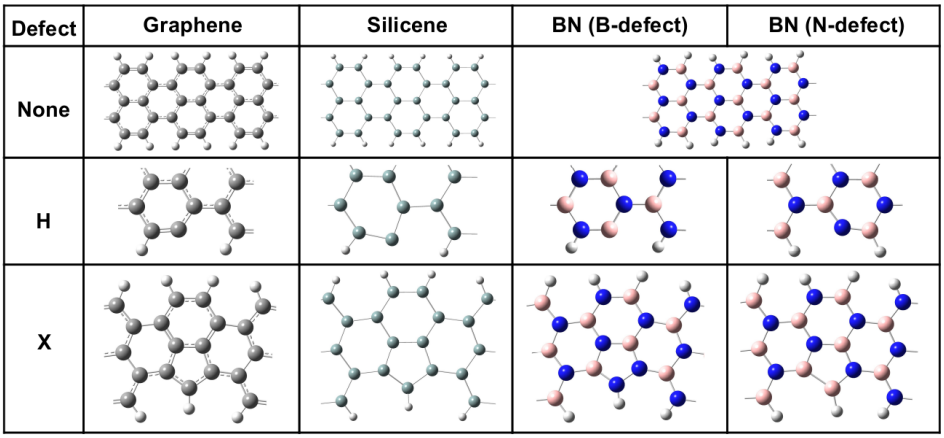

Figure 2: 42-atom junctions are displayed for pristine optimized nanoribbons. Magnified views of the region immediately surrounding each defect emphasize the local geometric changes. Boron atoms are pink and nitrogen atoms are blue in BN.

Following these geometry optimizations, force constant calculations were performed within Gaussian 09 using the same method and basis set to obtain

Hessian matrices, which contain the second derivative of energy with respect to position for each atom [69]. These matrices were used as input for an adapted version of the program TARABORD [72] that was developed to calculate phonon transmission coefficients (T_p) and densities of states (DOS) as functions of frequency [73–75], based on the non-equilibrium Green's function (NEGF) method that mathematically constructs an infinite open system with two semi-infinite pristine contact nanoribbons and a (defected) junction region in between:

$$G_{tM}(\omega) = [(\omega + i\eta)^2 I - K_C - \Sigma_L - \Sigma_R]^{-1} \tag{3}$$

$$T_p(\omega) = Tr[G\Gamma_L G^\dagger \Gamma_R] \tag{4}$$

$$DOS(\omega) = \frac{i\omega}{\pi} Tr[G - G^\dagger] \tag{5}$$

where ω is phonon frequency, n is a small real number, I is the identity matrix, and K_C is the junction Hessian.

The adapted program was verified by comparing its outputs to reported values for a polyethylene chain, with very good agreement observed [76,77]. These transmission coefficients were then used to calculate the phonon contribution to thermal transport at temperatures ranging from 1 to 500 K via the Landauer formula, an effective means to evaluate ballistic (i.e. collisionless) phonon contributions to thermal conductance κ_p in quasi-one-dimensional systems [78,79]:

$$\kappa_p(T) = \frac{\hbar}{2\pi} \int_0^\infty \frac{\partial f_{BE}(\omega)}{\partial T} T_p(\omega) \omega d\omega \tag{6}$$

where $f_{BE}(\omega)$ is the Bose-Einstein (B-E) distribution function. The function and its negative derivative are shown in Figure 3. While the distribution function can often be used in approximations to cut off a range of values that are unimportant for consideration in a given context, the magnitude of its derivative with respect

to temperature, as plotted here, doesn't fall off so quickly as to make the non-zero values at the higest frequencies seen in the systems here irrelevant.

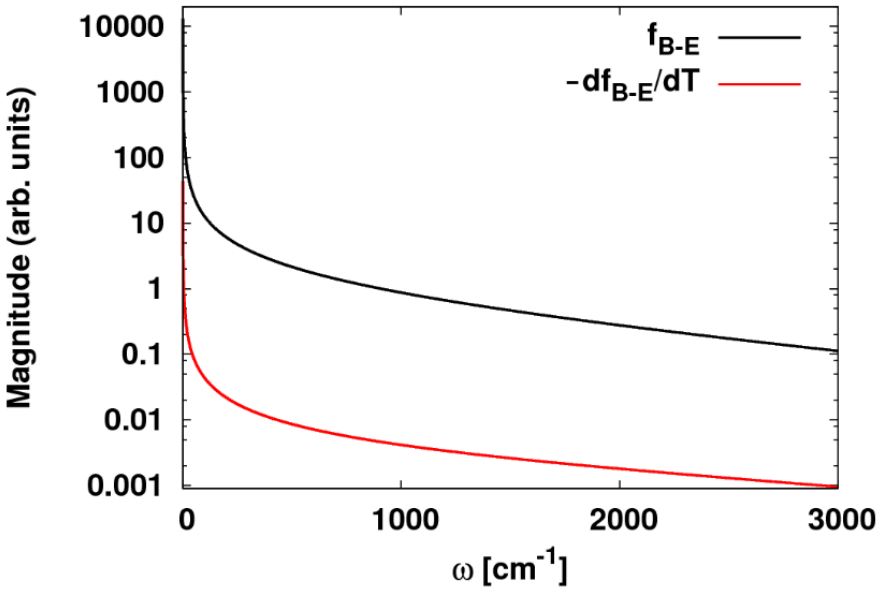

Figure 3: The Bose-Einstein distribution function and the magnitude of its negative derivative with respect to temperature at 300K as functions of phonon frequency.

The Landauer formula is suitable for this temperature range because anharmonic effects are not expected to be significant at or less than the maximum temperature of 500 K (or at 600 K, considered later). Ab initio studies have determined the strain at which anharmonic effects become significant in BN nanoribbons to be ∼0.1 [80]. Previous studies on graphene [81] and BN [82] structures have shown that variations of lattice parameters are much smaller than 10% for $0 < T < 600$ K. Furthermore, another study has shown that relative bond-length variations in lithiated silicene do not reach ∼10% or start to exceed it until the temperature reaches 900 K. [83] If 10% relative length variation is taken to qualitatively indicate the onset of significant temperature-induced anharmonic effects, then it is expected that those effects will not significantly change the conductance results over the temperature range considered here.

CALCULATING THE THERMOELECTRIC FIGURE OF MERIT

Hydrogen-passivated CNRs of two different widths $\lesssim 1$ nm for each of graphene,

BN, and silicene are considered here. One unit cell of each structure is shown in Figure 4. To assess electronic and lattice vibrational properties based on ab initio methods, structure optimizations were once again performed by (DFT) analyses employing the (B3LYP) method and 6-31G(d)[5] basis set in Gaussian 09 [63,64,69]. Clusters containing five unit cells and 192 atoms each were optimized for the narrow ribbons, while seven-unit cell structures with 250 atoms were optimized for the wider ribbons. Larger clusters were needed for wider ribbons because their greater width-to-length ratios necessitated the use of longer structures so that their central unit cells would effectively model those of infinite structures.[6] Hamiltonian, overlap[7], and force constant matrices were obtained following this optimization and input into the TARABORD program [72, 85–88] that calculates electron and phonon transmission coefficients (T_e and T_p, respectively) as functions of energy, using the ab initio-based NEGF method. Similarly to its approach to determining thermal conductance as described above, he method mathematically constructs an infinite open system with a junction consisting of one unit cell and semi-infinite contact nanoribbons consisting of periodically repeated structures to the left and right.

The electronic transmission is obtained using [89–91]

$$G_e(E) = (zS_J - H_J - \Sigma_{eL} - \Sigma_{eR})^{-1} \tag{7}$$

as

[5]This is a split-valence double zeta basis set with a single polarization function. 6-31G(d) is the conventional name for 6-31G*, which appears fairly commonly in the literature [84].

[6]Specifically, the program that was used to find conductance coefficients [72] was also used to find the Fermi energy of each structure; in all other structures, this was at the bandgap. In the 5-unit cell wide chevron graphene nanoribbon, it was reported as slightly away from the bandgap, but more problematically it varied in follow up runs made to confirm its placement. When 7-unit cell structures were considered instead, the Fermi energy was consistently identified as in the bandgap. This behavior may be worth further study at a later point; it has been speculated that one possible cause may be spin-induced magnetic effects from the bandgap edges in that particular graphene structure.

[7]Overlap matrices contain the basis vectors that describe how the orbitals of different atoms interact with one another.

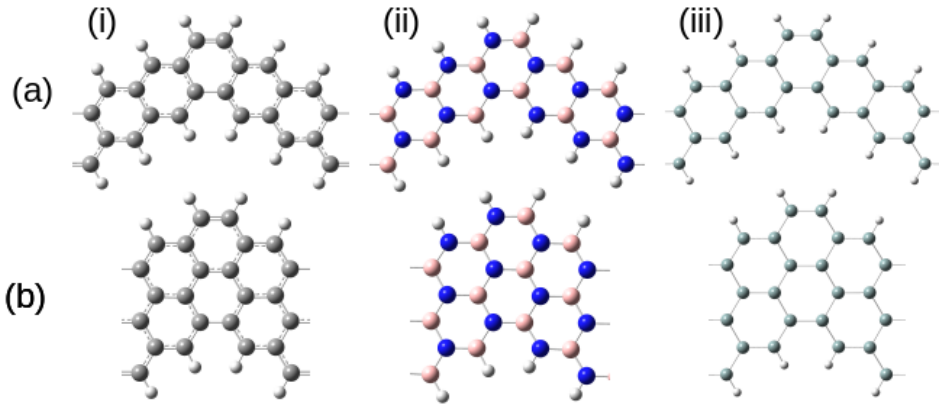

Figure 4: Unit cells of (a) narrow and (b) wide chevron nanoribbons made out of (i) graphene, (ii) boron nitride, and (iii) silicene.

$$T_e(E) = \mathrm{Tr}[\Gamma_{eL} G_e \Gamma_{eR} G_e^\dagger], \tag{8}$$

where G_e is the total electronic Green's function projected onto the junction unit cell, z is the complex energy, S_J and H_J are the overlap and Hamiltonian matrices corresponding to the junction unit cell, Σ_{eL} and Σ_{eR} are the electronic self-energies of the semi-infinite parts to the left and right sides of junction with Γ_{eL} and Γ_{eR} defined based on their imaginary parts, and T_e is the electronic transmission coefficient [72].

T_e is used to calculate the three electronic properties that factor into ZT (Eq. 1) [92, 93]:

$$\sigma = e^2 L_0(\mu, T), \tag{9}$$

$$S(\mu) = \frac{1}{eT} \frac{L_1(\mu, T)}{L_0(\mu, T)}, \tag{10}$$

and

$$\kappa_e(\mu) = \frac{1}{T} \left[L_2(\mu, T) - \frac{L_1(\mu, T)^2}{L_0(\mu, T)} \right], \tag{11}$$

where σ is electrical conductance, e is the electron charge, μ is the chemical po-

tential, T is the temperature, and $L_n(\mu, T)$ is the Lorenz function:

$$L_n(\mu, T) = \frac{2}{h} \int_{-\infty}^{\infty} T_e(E)(E-\mu)^n \frac{-\partial f_{FD}}{\partial E} dE, \tag{12}$$

with h and f_{FD} being the Planck constant and the Fermi-Dirac (F-D) distribution function, respectively. Figure 5 shows the F-D function and the magnitude of its derivative at 300K; like the B-E distribution function discussed above, it is also tool commonly used to make approximations, often acting as a function with values of either 1 or 0. Its derivative is generally very small but can nonetheless be relevant in these integrals, particularly when the function is zeroed in the center of a bandgap so all nonzero transmission coefficients are multiplied by a derivative value of a very low order of magnitude, or in L_1 where small asymmetries in an otherwise highly symmetric coefficient distribution could cause the sign of the intregral to change its term as energy changes slightly. The function is centered at zero and laid over one system's transmission coefficient distribution in Figure 19 to provide an example.

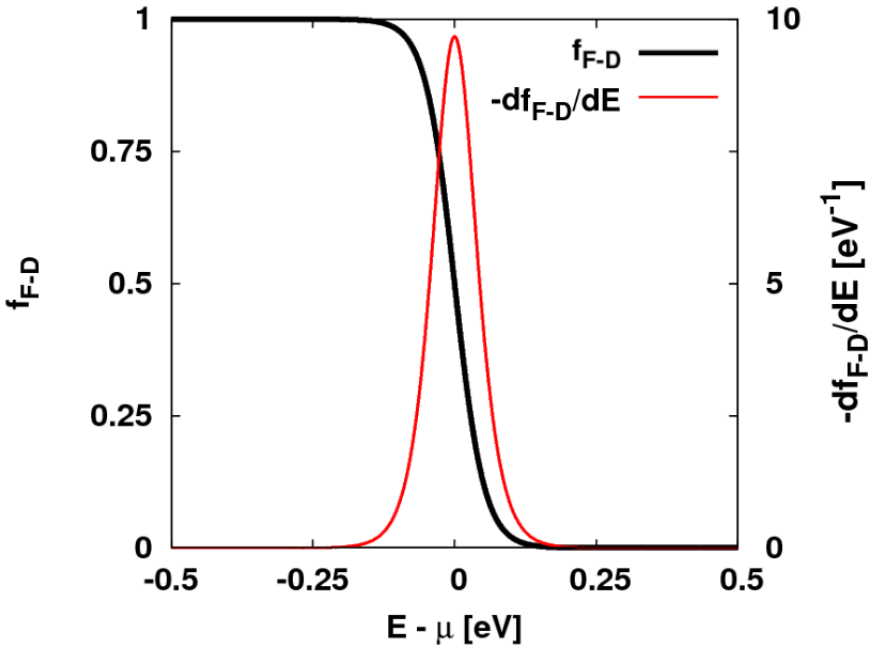

Figure 5: The Fermi-Dirac distribution function and its negative derivative with respect to energy at 300K as functions of difference from chemical potential, which is set to zero.

Following geometry optimization[8], force constant calculations[9] were also performed within Gaussian 09 once again using the B3LYP method and 6-31G(d) basis set to obtain Hessian matrices [69]. These matrices were used by TARABORD [72, 88] to calculate phonon transmission coefficients, T_p, as functions of frequency [73–75], based on the NEGF method, using equations 3 and 4. T_p values were then used to calculate the phonon contribution to thermal transport via the Landauer formula, as explained in the discussion surrounding and including 6.

$$\kappa_p(T) = \frac{\hbar}{2\pi} \int_0^\infty \frac{\partial f_{BE}(\omega)}{\partial T} T_p(\omega) \omega d\omega \tag{13}$$

where $f_{BE}(\omega)$ is the Bose-Einstein distribution function.

[8]In order for all calculations to converge, a stricter setting needed to be applied to the 7-unit cell wide silicene system. As part of any optimization run, the single point energy of the input geometry of a system is calculated before the actual optimization process begins. This single point energy calculation would not converge, and so an additional setting "scf=NoVarAcc" was included. VarAcc in Gaussian uses "modest integral accuracy" initially to conserve resources, and turning it off enforces the use of full accuracy from the beginning [94]. Furthermore, stricter settings yet needed to be applied to the wide 7-cell silicene optimization in order to obtain results that could be input into TARABORD to produce meaningful conductance coefficients; these were "Int(Acc2E=12)" and "Integral(Grid=UltraFineGrid)," which again call for more accurate calculations to be made [95].

[9]Force constant calculations of both graphene and silicene 7-unit cell wide chevron nanoribbons were very memory intensive and would terminate with an error message that could be linked to a memory allocation bug, which was fixed in revision E.01 of G09 [96]. These calculations were completed using that revision on the Owens cluster of the Ohio Supercomputer Center [97, 98].

IV. THERMAL CONDUCTANCE IN DEFECTED NANORIBBONS

GEOMETRICAL IMPACTS OF DEFECTS

Comparing optimized pristine structures to their optimized defected counterparts, as depicted in Figure 2, revealed many significant changes in the configurations of 14–, 13–, or 12-atom unit cells containing the defects. More subtle changes were also consistently seen in the unit cells immediately to the left and right of those containing defects. The pristine graphene ribbon was perfectly planar, with all angles generally close to 120° and with double bonds on its outer edges. Introducing a hydrogen defect caused the carbon atom, previously paired with hydrogen, to have an unpaired electron (or "dangling bond") and to move towards the center of the hexagon containing it, and to adopt a new angle of 127.5°. The nearest neighboring hexagon to the right was also distorted, as seen in 2 with a 126.9° angle introduced in its corner nearest the defect. The carbon defect caused a pentagon to form, containing all aromatic bonds. This pentagon caused the entire ribbon to adopt a slight V-shape with a 165.3° angle. Four single bonds were also introduced, with two connecting the defected unit cell to its neighbors and one fully contained within each of these neighbors. In all systems, double bonds range from 1.37 to 1.38 Å, aromatic bonds from 1.40 to 1.44 Å, and single bonds were consistently at 1.45 Å.

All BN NRs were perfectly planar, like graphene, and consisted of single bonds, like silicene. Defects concerning boron atoms produced different effects than those concerning nitrogen due to the different number of valence electrons in B and N. With its hydrogen lost, a B atom moves about 0.01 Å closer to each neighbor with the angle between them increasing marginally from 120.0° to 121.9°, while an N atom moves 0.02 and 0.04 Å closer to its neighbors and sees the angle in question increase from 123.6° to 133.1°. The X defects similarly produce a more symmetric structure for X=B; the pentagon corner consisting of B-N-N has bond lengths of 1.44 Å and 1.43 Å, whereas for X=N a heavily distorted B-B-N corner

with bond lengths of 1.75 Å and 1.44 Å is produced. That symmetry causes the B-defected NR to become the most severely bent at 164.3°, while the N-defected NR has a bend angle of 169.8°.

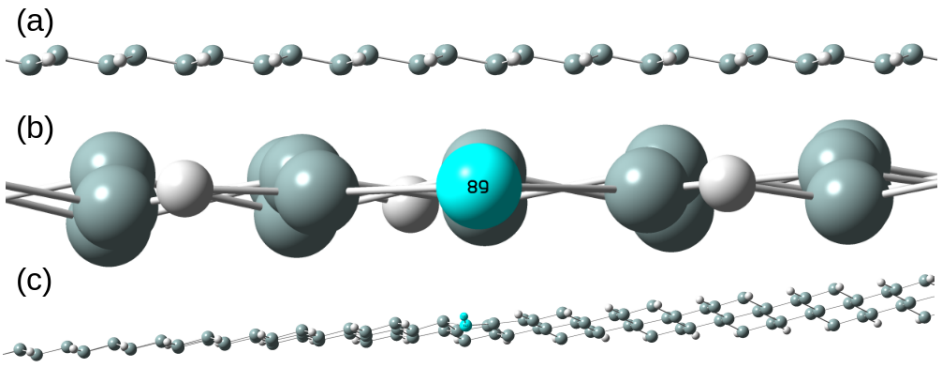

Figure 6: (a) The buckled structure of a pristine silicene nanoribbon, as viewed along its edge. (b) A hydrogen vacancy defect causes the silicon atom that it was attached to, which is highlighted and helpfully labelled "89," to lose its buckle relative to its neighbors and fall directly between them. (c) When a silicon vacancy defect occurs, the ribbon twists in opposite directions on the left and right of the buckle. The highlighted atoms (if viewed in color) are the silicon atom and its associated hydrogen that form a corner of the pentagon that is induced by the absence of a silicon atom.

Pristine silicene is also hexagonal but with single bonds and a buckle height of 0.54 Å, induced by its sp^2-sp^3 hybridization [99]. This buckle is displayed in Figure 6(a). Unlike in graphene, a hydrogen defect causes the associated silicon atom to move significantly outward, with its 117.4° angle to neighboring atoms dropping to 98.0° (i.e., its sp^3 hybridization is distorted to accommodate the unpaired electron present), with its edge and inner bond lengths extending from 2.22 Å and 2.28 Å to 2.29 Å and 2.31 Å, respectively. The nearest neighbor hexagon to the right also becomes distorted, with angle reduced to 111.5° at the atom nearest the defect. The silicon atom that had been bonded to the hydrogen becomes positioned directly between its neighbors with no buckle, as seen in Figure 6(b). A silicon defect again introduces a pentagon shape causing the ribbon to bend at 165.5°, with its smallest bonds at 2.25 Å between the innermost atoms of the pentagon and 2.24 Å connecting the pentagon to its upper neighbors. The buckled shape is maintained in this case, and it causes the ribbon to twist slightly

outwards in different directions on each side of the junction; see Figure 6(c).

TRANSMISSION COEFFICIENT IMPACTS OF DEFECTS

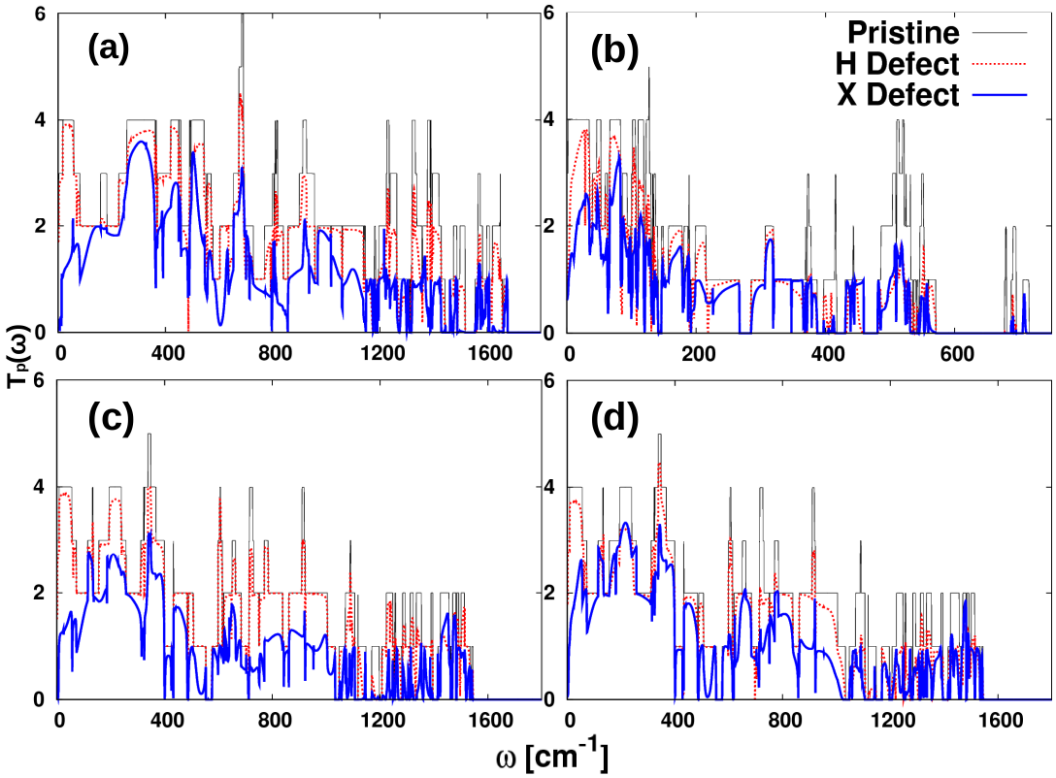

Figure 7: Phonon transmission coefficients as functions of frequency in pristine and defected graphene (a), silicene (b), and BN with B-defects (c) and N-defects (d). A few narrow hydrogen-induced units are not shown near 3200 cm^{-1} in graphene, 2600 cm^{-1} in BN, and 2200 cm^{-1} in silicene, as their contributions to conductance are negligible.

Calculated phonon transmission coefficients for each system are shown in Figure 7. Scattering of phonons by either defect reduces conductance across the entire frequency range, with the distorted geometries of the larger X defects producing more scattering [100]. This is in contrast to how simulations of much wider BN NRs than those considered here behave in response to larger internal defects; those defected structures display extreme reduction over a certain range of frequencies but none at low ones [101]. The cutoff frequencies, i.e., maximum frequencies whose conductance contributions are not negligible, for graphene, BN, and silicene are 1677, 1546, and 716 cm^{-1}, respectively. All systems share similar responses to defects across normalized ranges. This is particularly visible in X-defected struc-

tures at low frequencies, where defected structures gradually approach the four units of conductance that their pristine counterparts occasionally reach, before tapering back down. All systems also show numerous reductions to zero in the upper portions of their frequency ranges.

MECHANISMS EMERGING ALONGSIDE THERMAL CONDUCTANCE LOSSES

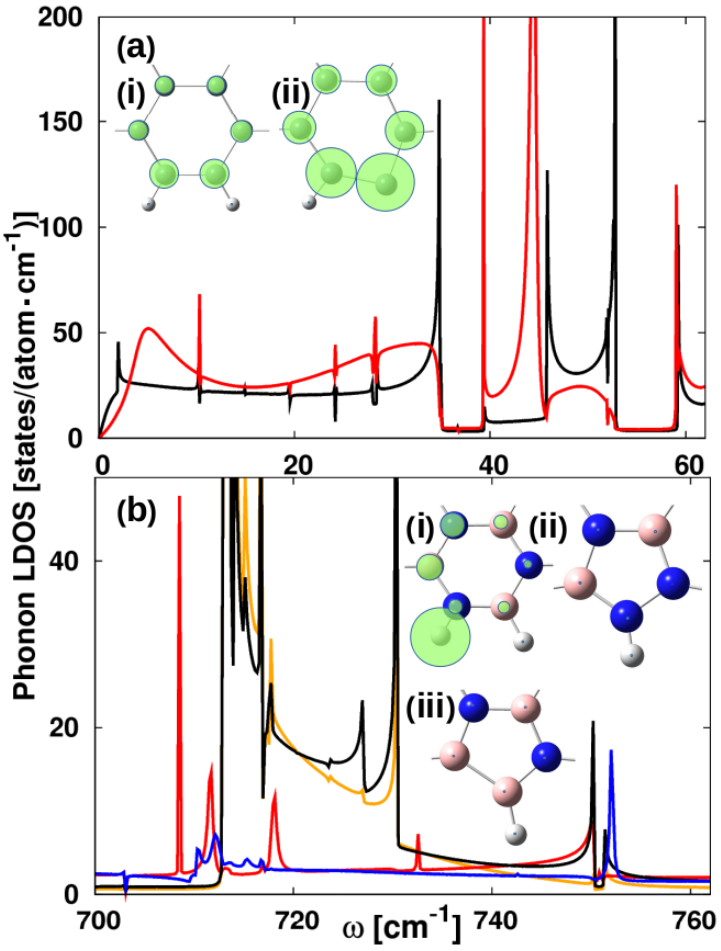

Figure 8: Local phonon densities of state (LDOS) for atoms at defects for selected frequency ranges in (a) silicene and (b) BN NRs. Insets show normalized LDOS values in (i), pristine and (ii, iii) defected NRs near defect at 4.6 cm^{-1} in silicene and cm^{-1} in BN. In (a), curves are for the Si atom that loses its H; black is pristine and red is defected. (b) considers atoms that will be lost when an X defect occurs; black and orange are N and B, respectively, in pristine BN; blue and red are N (ii) and B (iii), respectively, that remain when their counterpart is removed.

Two major mechanisms that emerge in correspondence with conductance losses are demonstrated in Figure 8 for silicene and BN NRs. In the case of a hydrogen defect (Figure 8(a)), a broad local phonon densities of state (LDOS) peak emerges at 310

cm^{-1}, coinciding with the defected system's markedly low, gradually increasing values of conductance seen in Figure 7(b). This peak indicates a flexible center, i.e., with increased LDOS compared to the pristine case, causing phonon scattering that reduces thermal transport across the NR. Similar incomplete geometries cause these peaks to emerge in all other hydrogen-defected NRs, though they were most pronounced in silicene, where bonds near the defect weaken, thus allowing localized vibrations resulting in increased LDOS. Figure 8(b) shows an opposite phenomenon, where the bonds near the defect strengthen causing diminishment of vibration modes and an LDOS drop by an order of magnitude in defected structures at some frequencies. Emergence of such stiff scattering centers impedes phonon conductance across the NR. These changes vary depending on which atom is removed, as one can see by comparing the black-blue (N atom) pair of curves to the orange-red (B atom) pair. The flexible scattering centers localize phonons at the defect, while stiff ones delocalize them, instead localizing them onto the edges of the structure away from the defect, as was confirmed by checking the LDOS of all atoms in the junctions of the defected structures as compared to those in the pristine ribbons. The defects, therefore, act as phonon localization/delocalization centers. Such geometrical irregularities with corresponding phonon disturbance as compared to the pristine nanoribbon's phonon LDOS cause scattering centers for phonons resulting in conductance reduction. Comparatively, there is no scattering in the pristine nanoribbons where each phonon band contributes exactly one unit of transmission, and the transmission curves depicted in Figure 7 specify the amount of scattering for each phonon mode (energy) for each defect in different structures.

THERMAL CONDUCTANCE LOSSES AT 300 K

The conductance values found for each pristine structure at 300 K (as depicted in Figure 9) are on the same order of magnitude as those previously reported in the literature although they are consistently smaller. This is due to the different methods used [5, 18, 102]. Generally speaking, these thermal conductance values

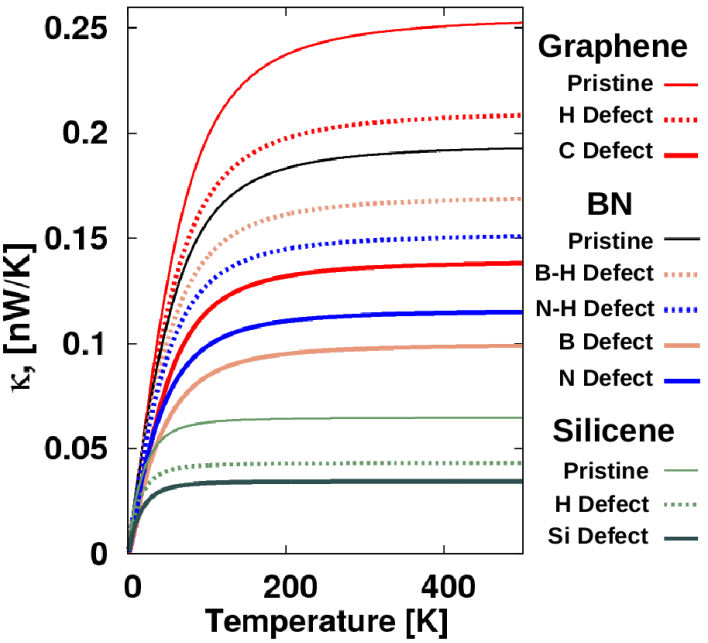

Figure 9: Thermal conductance for pristine and defected nanoribbons as a function of temperature.

are relatively small in all cases. This is because phonon-boundary scattering is the limiting factor in systems with small diameters, up to around 50 nm [30]. Smaller diameters result in smaller conductances yet; this is the reason for the low conductances in these nanoribbons, which have widths less than 1 nm.

Figure 9 demonstrates that a single defect in graphene can reduce its ordinarily high conductance to less than that of its analogue BN, to the extent that introducing a C-defect into graphene will make its conductance even less than BN with an H-defect. Reductions in BN are quite different depending on whether a defect occurs at a boron or nitrogen atom, which is true whether it is H or X type. If B-H and N-H or B- and N- defects could be expected to occur with similar probabilities, this would introduce further uncertainty to a BN NR's expected performance. At 300 K, H defects cause reductions between 12% and 21% in graphene and BN. The reduction in silicene is particularly high at 33%, due to features like its pronounced peak in Figure 8a. This peak is particularly impactful since it occurs at a low frequency, where the B-E derivative is one or two orders of magnitude greater than over much of the remaining range (see Figure 3. It

is worth keeping in mind, however, that silicene's H curve in Figure 7(b) is less similar to its analogue than any other pair; this corresponds to its buckled structure with one non-buckled segment being unique among the H-defected systems considered here.

All systems show losses of 40%–48% when an X defect is introduced; this is supported by Figure 7 where all blue (X-defect) curves have qualitatively similar normalized shapes with greater reductions at low frequencies corresponding to the greatest losses. Some previous studies on thermal transport in defected graphene patches, using molecular dynamics based on empirical potentials, reported larger decreases [103–106]. These greater values were found because they considered large concentrations of defects rather than the single point defects in otherwise perfect nanoribbons that were studied here. The different reductions in BN presented in Figure 9 when N and B are removed are because of the LDOS variations discussed above: N-N pairs form a strong bond with each other (1.43 Å) compared to B-B (1.77 Å), and that stronger bond causes greater suppression of vibrations in B-defected BN.

V. THERMOELECTRIC PERFORMANCE IN CHEVRON NANORIBBONS

ZT IN GRAPHENE, BORON NITRIDE, AND SILICENE CHEVRON NANORIBBONS

Thermoelectric properties were calculated for each CNR at temperatures of 300 and 600 K as functions of chemical potential. For pristine and unbiased systems, the intrinsic Fermi energy was taken to be at the center of the electronic band gaps present in all six systems. For doped and/or biased systems, the chemical potential can deviate from that Fermi energy in the center of the gaps. In the following discussions, the intrinsic Fermi energy is shifted to zero. Figure 10 demonstrates how thermoelectric properties change with respect to chemical potential in narrow and wide silicene systems at both temperatures. While this sample has a high concentration of ZT peaks over a small energy range, it displays a feature that is generally seen in all systems at both temperatures; ZT has many peaks situated along ranges where the Seebeck coefficient is relatively large while electron-contributed thermal conductance is relatively small.

From Figure 10, one notices that silicene displays asymmetries in its ZT behavior when it is p- rather than n-doped. Higher ZTs are generally found at negative Fermi energies, though more small peaks are present at positive ones. Owing to its small band gap and low phonon thermal conductance, ZTs greater than three are found for both widths at both temperatures within ± 1 eV of the center of the gap. This would be beneficial in cases where small changes in Fermi energy are desirable through moderate doping or bias. Silicene CNRs also show relatively more frequent Seebeck coefficient peaks per energy, resulting in more ZT peaks relative to graphene and BN (see Figures 20 and 21 in the Appendix). The ZT peaks in silicene are generally higher than those in other systems due to relatively low phonon-contributed thermal conductance. Despite the explicit dependence of ZT on temperature in Eq. 1, the ZT peaks at 600 K are less than double the corresponding 300 K ones, owing to reduction of the Seebeck coefficient and increase of κ_p. Therefore, identifying materials and system geometries with

properties conducive to high thermoelectric performance at room temperature is an approach that should be preferred over simply increasing temperature to maximize ZT. High Seebeck coefficients within the band gap that do not coincide with nonzero electrical conductance are not relevant for thermoelectric purposes. That said, the narrowing of the band gap at high temperatures does mean that the ZT peak nearest the band gap will become taller and wider as a result.

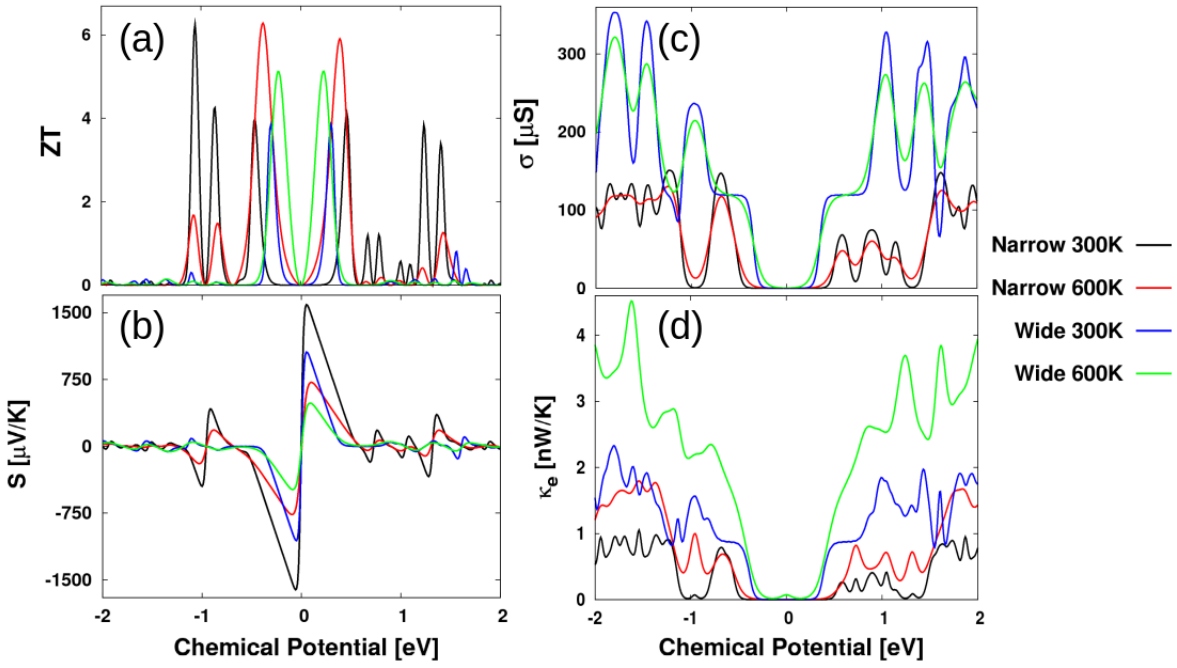

Figure 10: Thermoelectric properties of narrow and wide chevron silicene nanoribbons near the band gap, at 300 and 600 K. Intrinsic Fermi energy, i.e. that of pristine and unbiased systems, is at the center of the gap and shifted to zero.

For graphene CNRs, the results here show that the effects of changing chemical potential are largely similar at 300 and 600 K, and are fairly symmetrical on both sides of the band gap; they are almost completely symmetrical in the wide nanoribbons. In both systems, almost no variation is seen in electrical conductance between temperatures. However, the peaks surrounding Seebeck coefficient sign changes are more pronounced at 300 K than at 600 K, and thermal conductance peaks are seen to approximately double with temperature, with slightly higher increases at negative Fermi energies. Of note is that there are p-type peaks and n-type peaks having nearly equivalent ZTs and Fermi energies with oppo-

site Seebeck coefficient signs in both graphene systems, which may enhance the flexibility of graphene CNRs in engineering applications. As for BN CNRs, the thermoelectric properties vary somewhat more as Fermi energy changes relative to those of graphene. ZT has a more asymmetric nature in BN on each side of the band gap; we see no peaks in any BN system between -6 and -4 eV, but four peaks are observed in narrow BN from 4 to 6 eV (see 23 in the Appendix). At these high Fermi energy levels the narrow BN CNR actually performs slightly better at the lower 300 K, owing to a combination of Seebeck coefficient sign changes and very low electron-thermal conductances, both of which are much less pronounced in the wide BN CNR. As was the case with graphene, electrical conductance shows little variation with temperature per system, though the peaks for BN CNRs do show greater differences than in graphene at different temperatures.

Maximum ZT values within 5 eV of the band-gap center, together with corresponding thermoelectric characteristics, are shown in Table 1 for all systems. In general, high ZTs are found in systems with low phonon-contributed thermal conductance, which changes with temperature but not Fermi energy, and thus serves as a limiting factor in figure of merit calculations.

COMPARING CHEVRON NANORIBBONS TO STRAIGHT NANORIBBONS

As mentioned before, CNRs have a high edge to surface area ratio that can reduce κ_p owing to phonon-boundary scattering. In order to assess how κ_p in graphene CNRs compares to that in non-chevron ribbons, two options are available: to compare with very thin zig-zag edged nanoribbons (ZNR) that make up the straight sections of CNRs, or to compare with slightly wider armchair-edged nanoribbons (ANR) that CNRs could be carved out of. For the two options corresponding to the narrow graphene CNR considered here, Tomita et. al find in a first-principles study that the phonon- contributed thermal conductance of 2-atom wide ZNRs as well as 6-atom wide ANRs are both close to 1 nW/K [54]. Here, values of 0.142 nW/K and 0.198 nW/k were found for narrow and wide graphene CNRs, respectively, supporting the idea that the introduction of a chevron structure in

Table 1: Thermoelectric properties of narrow and wide graphene, BN, and silicene chevron nanoribbons at 300 K, at chemical potentials where maximum ZT values occur within ± 5 eV from the center of the band gap (set at zero). Two p-type maxima are given for wide silicene; the larger one is both remarkably high and far from the bandgap center, unlike that of the other systems.

System	μ [eV]	Max ZT	$\sigma[\mu S]$	S [μV/K]	κ_e [nW/K]	κ_p [nW/K]
Narrow C	-1.99	2.44	21.1	264	0.0379	0.142
	2.01	2.45	23.2	-254	0.0421	
Narrow BN	-3.65	2.74	23.5	-236	0.0373	0.106
	4.84	3.09	25.1	-242	0.0363	
Narrow Si	-1.06	6.26	14.1	-300	0.0271	0.0338
	0.46	4.13	9.10	271	0.0146	
Wide C	-0.69	1.05	14.6	-232	0.0273	0.198
	0.69	1.05	14.6	232	0.0273	
Wide BN	-3.26	1.22	14.2	-235	0.0265	0.166
	3.94	2.78	42.6	-233	0.0830	
Wide Si	-4.66	8.01	28.3	312	0.0441	0.0590
	-0.30	3.85	13.5	-281	0.0239	
	0.3	3.84	13.5	281	0.0239	

place of a straight one can reduce phonon-contributed thermal conductance considerably. This is an even greater reduction than that found by a study using a tight binding (TB) methodology, which suggested a threefold decrease in room temperature phonon thermal conductance in CNRs relative to straight ones, for a wider nanoribbon [38]. Another study provides data on thermal conductance in BN ZNRs and ANRs; their data also reports κ_p near 1 nW/K in 2-atom wide BN ZNRs, and through extrapolation of their reports on many systems, values near 1 nW/K are also expected in 3-ZBNNRs and 6- and 7-ABNNRs [102, 107]. The values of 0.106 and 0.166 nW/K reported here for narrow and wide BN systems further suggest that this chevron pattern causes diminished thermal conductance. Since reducing phonon-contributed thermal conductance is a primary means of increasing ZT, as discussed above, this provides further support for the idea that chevron structures are well-suited for thermoelectric applications. Other studies are available that have found higher figures of merit in unaltered, i.e. straight, armchair nanoribbons due to lower corresponding phonon-contributed

thermal conductances, e.g. κ_p of 0.028 nW/K in a 5-atom wide armchair NR [40] compared to the 0.247 nW/K that we found in a previous study [88]. However, the results are not directly comparable due to the different methodologies used; phonon calculations based on classical potential compared to the ab initio B3LYP calculations made here; it is suspected that the method used there would similarly find an even lower thermal conductance in a chevron structure relative to a straight one.

Beyond considerations of only thermal conductance, another previous study also used a fully quantum approach to compare phonon thermal conductance, electrical conductance, Seebeck coefficient, and ZT between straight and chevron graphene nanoribbons with both armchair and zigzag edges [68], although they looked at wider ribbons than those considered here and did not report ZTs at or above unity as is the case here. Another recent study assessing silicene nanoribbons, but with TB methods, found that the introduction of edge defects can lead to up to a 2.48-fold increase in ZT over the pristine case [18]. Two other TB studies have also qualitatively explained why edge disorder allows for high ZTs in defected graphene nanoribbons, while quantitatively comparing phonon-contributed thermal conductance and electronic conductance in edge-defected nanoribbons to that of a pristine ribbon, in both wide ribbons [108] and those with widths comparable to those considered here [109]. Others yet have compared phonon transmission coefficients of straight graphene nanoribbons to those in chevron ones via TB [52], compared phonon thermal conductance as a function of width in pristine ribbons to that of ribbons with various densities of edge defects with a linearized Boltzmann approach [110], and assessed edge modulation in larger γ-graphyne NRs to find that ZT could improve by a factor of approximately 1.5 relative to a perfectly straight ribbon, by using the Brenner potential [111]. The results presented here show that by considering smaller widths and a variety of materials, it is possible to achieve systematic enhancement of figure of merit based on accurate ab initio calculations, considering the effects of quantum transport described earlier..

GENERAL OBSVERATIONS OF ZT BEHAVIOR

Some general observations and comparisons of ZT components are as follows: In all systems, electrical conductance as a function of chemical potential remains fairly constant with regard to temperature, while electron-contributed thermal conductances invariably rise. Electrical conductance changes very little in graphene of either width at different temperatures, while in BN and silicene it tends to fluctuate more at low temperatures, especially in wider structures. The Seebeck coefficient varies less with energy at higher temperatures and widths across systems. Width suppresses S more than temperature in graphene and BN, while temperature has a greater impact than width in silicene. The graphene ribbons show very few ZT peaks more than ± 3 eV from the center of the band gap because their Seebeck coefficients rarely vary when away from the gap, even at energies where the ratio of electrical conductance to electron-contributed thermal conductance is relatively high. Their possession of the highest phonon thermal conductance of any of our systems makes this unfavorable ratio additionally difficult to overcome. These graphene systems have similar values of maximum ZT when compared to the highest reported values from studies of other engineered nanoribbons at 300 K based on a quantum approach [38, 39]. The narrow BN ribbon is expected to perform slightly better, and the narrow silicene ribbon exceeds both of those by more than a factor of two while also surpassing that of the best-reported quantum-analyzed silicene ribbon [45]. In BN, the wider system generally has large ranges of high κ_e with few reductions to the order of magnitude of its κ_p, causing it to have figures of merit consistently lower than its narrow counterpart, with a notable exception near +4 eV, where low electron-contributed thermal conductances in the wider system result in ZT peaks that do not exist in the narrow ribbon. These ZT peaks do not occur right at the edge of the bandgap but are also not far from it, which is a unique feature among the three wide NRs that we considered. The variation of width in silicene produces two features not seen in other systems. Relatively large Seebeck coefficient peaks ± 10 eV from the

center of the bandgap in narrow silicene are, especially at negative Fermi energies, often fairly closely aligned with Seebeck magnitude in wider silicene NRs; this behavior is uncommon in graphene and BN. And, interestingly, the highest calculated ZT value within ± 5 of the gap is in wide silicene at 300 K, where it exceeds 8 at -4.66 eV, due to the confluence of a notably high electrical conductivity and Seebeck coefficient while the electron-contributed thermal conductance is slightly less than that contributed by phonons.

FULL-WIDTH AT HALF-MAXIMUM ZT PEAK BEHAVIOR

Full-width at half-maximum (FWHM) values of ZT peaks versus chemical potential indicate sensitivity of the peaks to small changes in doping and/or bias. Values of FWHM are approximately 0.09 eV for all systems at 300 K and 0.19 eV at 600 K; the largest deviation from this is in n-type narrow BN, which has a FWHM of 0.15 eV [at 600 K]. This suggests that they are generally more dependent on temperature than system width or material, and that materials where chemical potential may be prone to fluctuations are better suited for deployment at high temperatures, in order to maintain high ZTs.

EFFECTS OF P- AND N- TYPE DOPING

Systems that can have high ZTs on either side of the band gap have additional value for real-world applications; Figure 11 displays all systems' maximum values when they are (a) p-type and (b) n-type doped. One feasible method of doping would be introducing physisorbed dopants which would not change the electronic properties of the system in the way that covalently bonded dopants would, e.g. tetracyanoquinodimethane (TCNQ; p-type) or tetrathiafulvalene (TTF; n-type) in silicene [45]. Identifying particular adsorbtion candidates require special care, as it was previously found that absorption of a single CO molecule on a pristine silicene NR significantly alters its quantum conduction [112].

In these systems, similar ZT magnitudes are most commonly seen regardless of type of doping. However, wide BN has a high ZT at 300 K when it is n-type doped, a peculiarity that could lend it appeal over a system like narrow graphene,

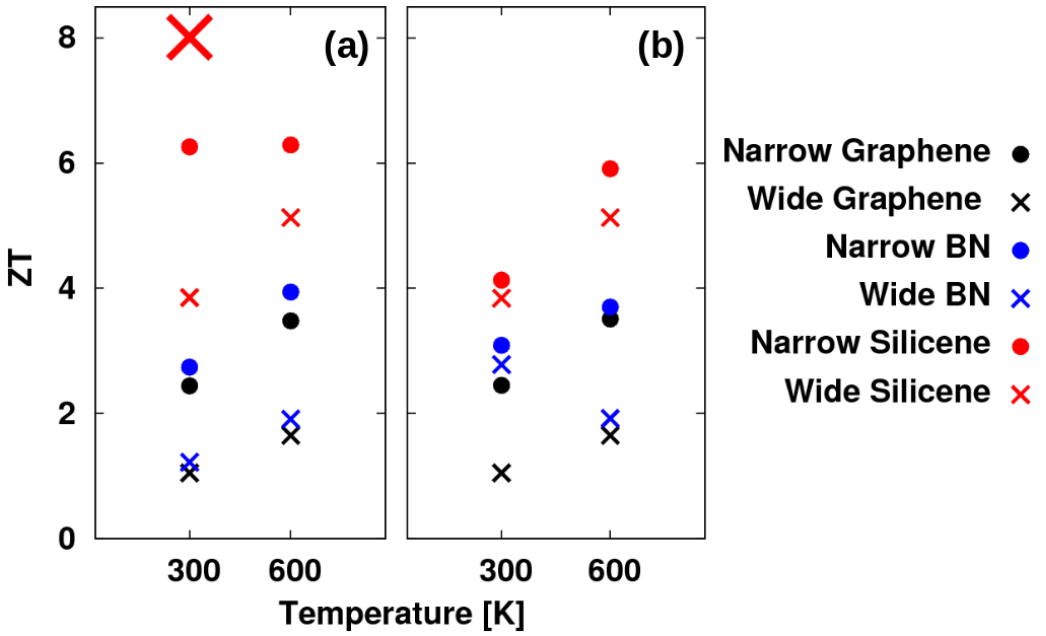

Figure 11: Variation in maximum thermoelectric figures of merit under p-type doping (a) and n-type doping (b) with respect to temperature, for narrow and wide graphene, BN, and silicene nanoribbons, within a chemical potential of ±5 eV from the intrinsic Fermi energy (centered in the band gap, and set at zero). Maximum ZT peak occurs for p-type wide silicene and happens far from the gap, unlike other peaks that occur near the band gap edge.

which otherwise generally performs better. Interestingly, silicene displays some variations, with its narrow system having approximately the same p-type maximum ZT at 300 and 600 K, whereas it displays the expected behavior of increasing with temperature when n-doped. Wide silicene behaves typically near the edge of its band gap, but also has a a figure of merit greater than that found in any of the other systems within ±5 eV of the gap, near -5 eV. Besides its magnitude, this value is unusual in that it occurs in both a wide structure and at at lower temperature. It should be noted that this relatively high value is achieved near the end of this range of chemical potentials, and by considering an even wider range like ±10 eV, relatively large ZT peaks do emerge far from the gap in other systems. In this expanded range, silicene continues to consistently outperform the other two materials, and the very highest value of all systems at these two temperatures is in narrow silicene at 600 K, in line with our expectations, at 8.71 at -8.91 eV.

ZT COMPONENT IMPACTS ON *ZT* MAGNITUDE

Another consideration regarding practical applications is the sign of the Seebeck coefficient, which is irrelevant for the calculation of figure of merit but is related to the directions of thermal and electric current. Sample Seebeck coefficients at 300 K are provided in Table 1. Seebeck coefficient signs associated with maximum *ZT* at one temperature and chemical potential will not necessarily be the same at others because the variation of those two will cause these peaks to shift, emerge, or diminish. A material-specific feature that can affect *ZT* is application of an external electric field; this can widen the band gap of a silicene NR, but not in a graphene one [113–115]. This could shift the *ZT* peaks away from the energy where one would otherwise expect to see them.

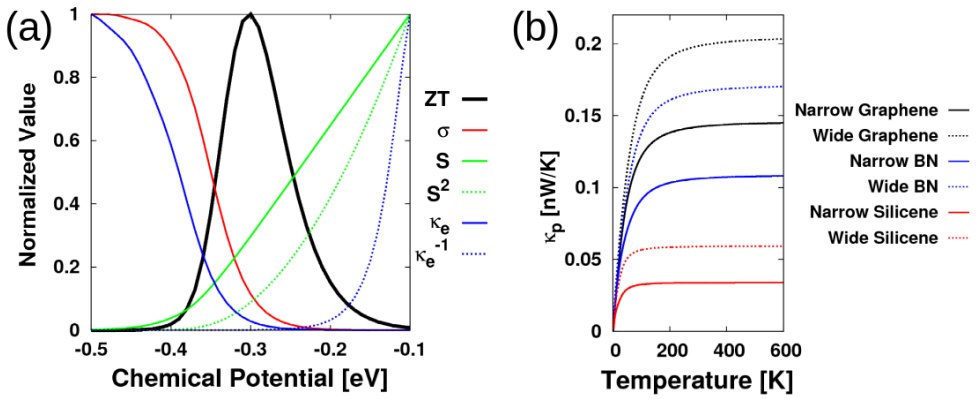

Figure 12: (a) Normalized values of the thermoelectric figure of merit and its components near the peak at -0.3 eV in narrow silicene CNR at 300 K. (b) Thermal conductance for each system as a function of temperature.

Figure 12(a) displays how a typical high *ZT* peak, specifically the peak at -0.3 eV in narrow silicene CNR at 300 K, emerges as a result of its components' behavior. Each plotted component is normalized based on its behavior from -0.5 to -0.1 eV, where 1 is its maximum value across that range (these values can be found in Table 1). One factor contributing to the presence of a *ZT* peak is proximity to a Seebeck coefficient peak, regardless of whether *S* is increasing or decreasing, or is positive or negative. The second factor is proximity to electrical and electron-contributed thermal conductance shifting away from one another as Fermi energy changes. These two generally increase or decrease along with each

other, but some differences can be observed, such as greater variance at a peak in thermal conductance relative to the corresponding peak in electrical conductance, or the apparent lag effect seen here. When this happens, a ZT peak will emerge at the intersection of normalized σ and S^2, the two terms that directly enhance the figure of merit. Higher ZT peaks will occur in instances where this lag behavior occurs closer to a Seebeck coefficient peak.

Phonon contribution to thermal conductance depends only on temperature, as shown in Figure 12(b). This limits the maximum ZT that can emerge when its other components interact as was just described. As Table 1 indicates, ZT peaks consistently occur at energies where electron-contributed thermal conductance is less than the phonon contribution. As is seen in Figure 10(d), the rarity of this occurring limits the number of high ZTs that can occur across an energy range. Figure 12(b) clearly shows that choice of either width or material can be the factor that results in a higher phonon-contributed thermal conductance. Silicene has lower phonon-thermal conductance than any graphene or BN system, but a narrow NR of either graphene or BN will have a lower conductance than a wide one.

VI. CONCLUSIONS

Edge defects in narrow nanoribbons will affect thermal conductance similarly in systems that share geometries. Hydrogen losses will reduce conductance more when they distort the geometry of a system, like they do when removing the buckle in silicene. Losses of larger atoms will consistently cause greater losses than hydrogen defects. Emergence of flexible scattering centers at defects, with increased local densities of states compared to the pristine case, can be expected to show greater conductance losses when new bonds are weaker. On the other hand, when stiff scattering centers with reduced local densities of states are introduced at defects, stronger bonds result in greater resistance to transport. This knowledge could be useful in applications utilizing thermal transport in novel nanoribbons, through crafting expectations of how defects may affect performance, in particular when an understanding of those changes is known in an analogue system.

All six systems had thermoelectric figure of merit peaks distributed near the edges of their band gaps; the magnitudes of these peaks were usually greater in narrow systems, and were consistently highest in silicene and lowest in graphene. Choosing width or material to optimize a system's performance may depend on which systems are being compared- while choosing silicene over the other two materials always resulted in a higher ZT, either width or material could be the property of paramount importance if just choosing between graphene and BN. Even greater ZT values can be found far from the band gap, but far enough away that changing the chemical potential that much could change the system's electronic properties and result in shifting or rounding down its ZT peaks. The highest near-band gap ZT of 6.26 in narrow silicene at 300 K suggests that it holds particular promise for thermoelectric applications. The narrow BN and wide

silicene systems also surpass 3, a benchmark value for thermoelectric materials to overcome to be considered efficient at converting heat to electricity. The knowledge of how these nanoribbon widths and materials affected ZT could be instrumental in making decisions about materials to incorporate in thermoelectric generators.

VII. APPENDIX

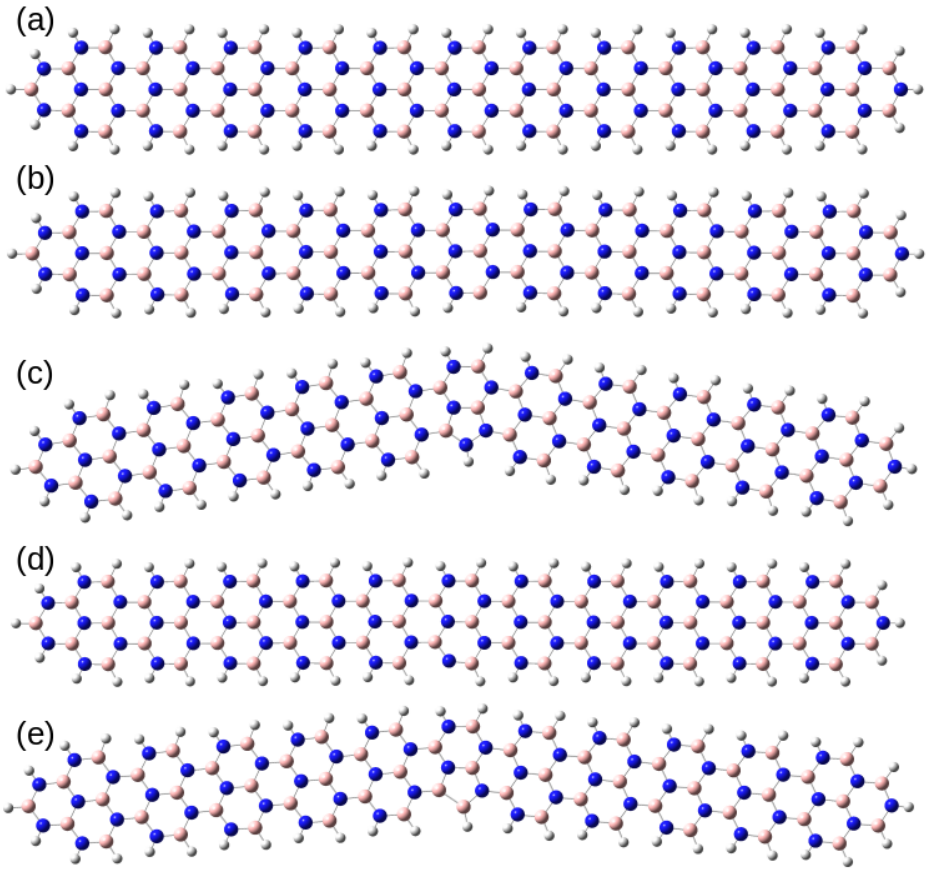

Figure 13: Optimized segments of hydrogen-passivated BN nanoribbon in (a) pristine case, (b) with a defect created by removing a single hydrogen atom that had been bonded to a boron (pink) atom, (c) with a defect created by removing a single boron atom, (d) with a defect created by removing a single hydrogen atom that had been bonded to a nitrogen (blue) atom, (e) with a defect created by removing a single nitrogen atom.

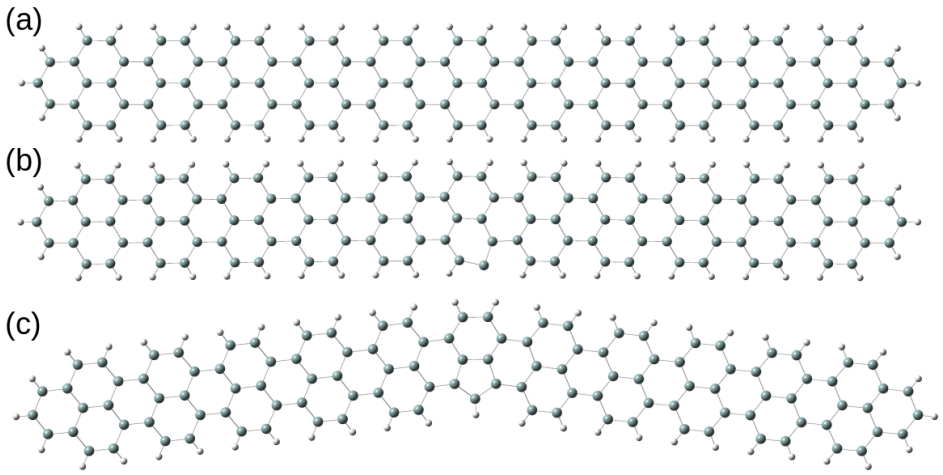

Figure 14: Optimized segments of hydrogen-passivated silicene nanoribbon in (a) pristine case, (b) with a defect created by removing a single hydrogen atom that had been bonded to a silicon atom, (c) with a defect created by removing a single silicon atom.

Table 2: Energies of Optimized Pristine/Defected Nanoribbons [H]

System	Graphene	BN (B-defect)	BN (N-defect)	Silicene
Pristine	-4450.959	-4653.409		-33610.992
H-Defect	-4450.276	-4653.730	-4653.718	-33610.378
X-Defect	-4412.213	-4627.806	-4597.932	-33320.892

Energies of pristine and defected nanoribbons following optimization. Intramaterial comparisons can be made to assess single defect impacts on system stability.

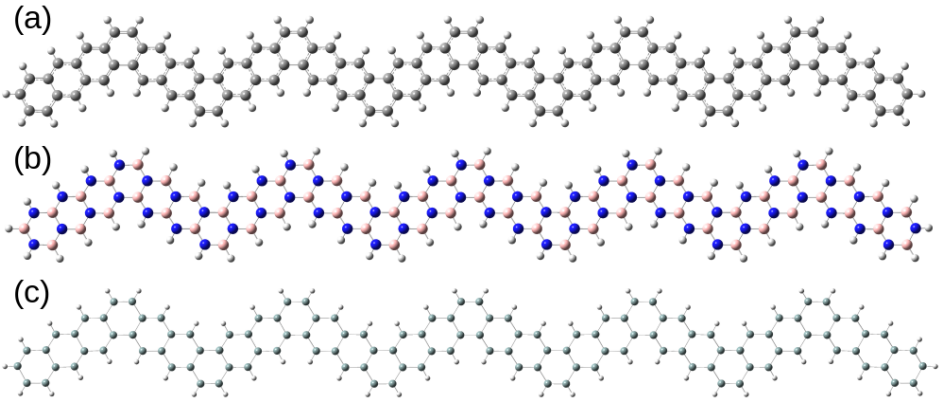

Figure 15: Optimized segments of 5-unit cell narrow (a) graphene, (b) BN, and (c) silicene chevron nanoribbons.

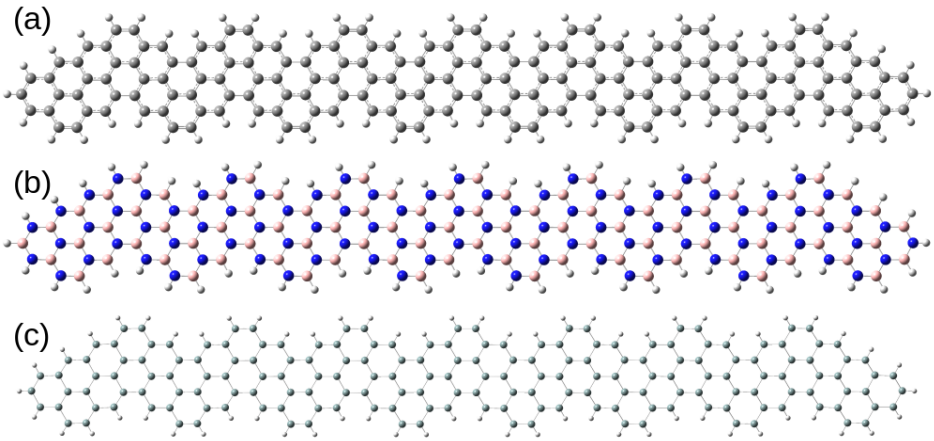

Figure 16: Optimized segments of 7-unit cell wide (a) graphene, (b) BN, and (c) silicene chevron nanoribbons.

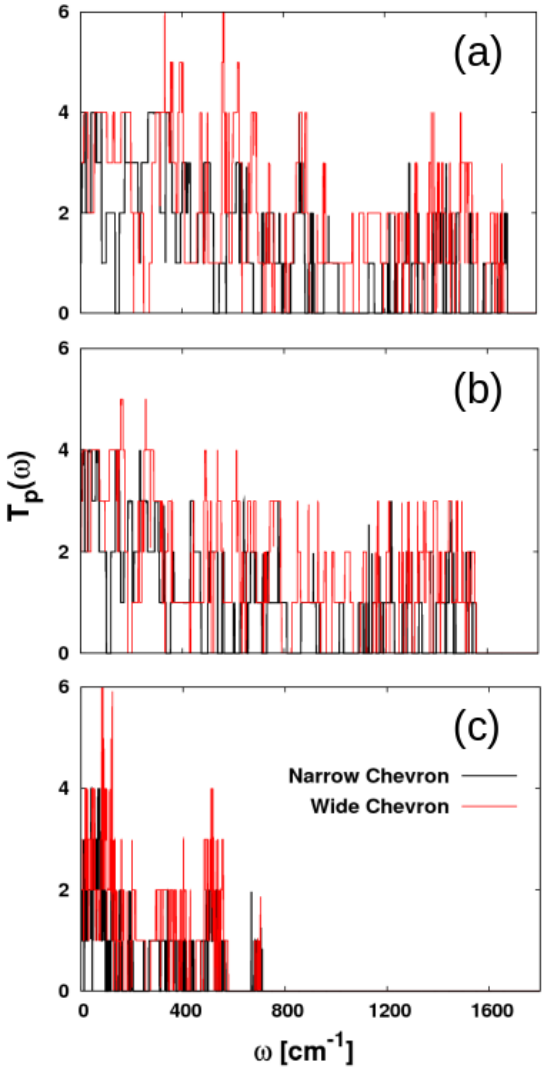

Figure 17: Phonon transmission coefficients of (a) graphene, (b) BN, and (c) silicene chevron narrow and wide nanoribbons. A few non-zero transmission coefficients are omitted near 3200 cm^{-1} in graphene and near 2650 and 3600 cm^{-1} in BN.

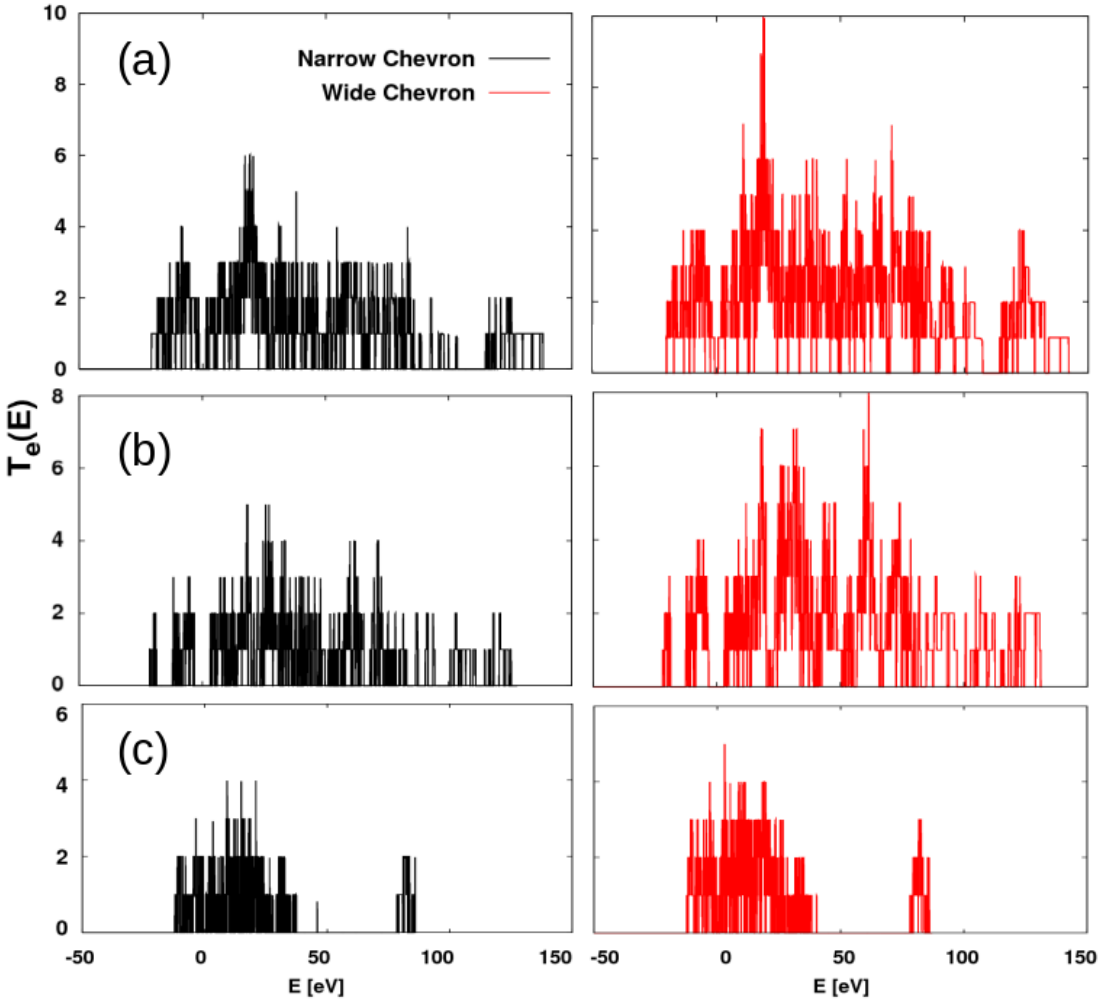

Figure 18: Electron transmission coefficients of (a) graphene, (b) BN, and (c) silicene chevron narrow and wide nanoribbons. A few non-zero transmission coefficients are omitted near -274 eV in narrow and wide graphene, -386 in wide BN, and -95 eV in narrow and wide silicene.

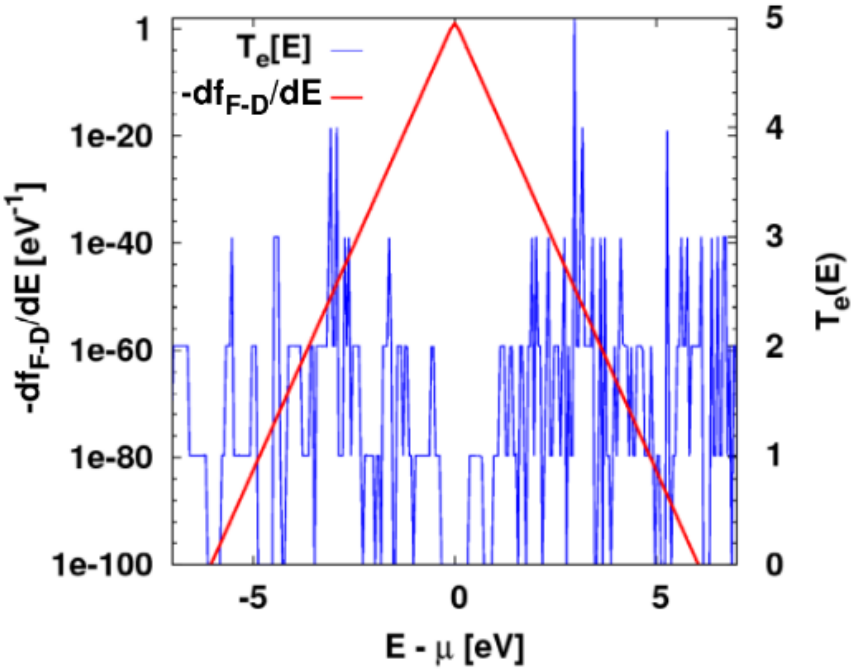

Figure 19: Electron transmission coefficients for the wide silicene chevron nanoribbon and the negative derivative of the Fermi-Dirac distribution function with respect to energy at 300K as functions of chemical potential near the Fermi energy, which is set to zero in the center of the ribbon's bandgap.

Table 3: Thermoelectric Properties of Chevron Nanoribbons at Max ZTs at 600 K

System	μ [eV]	Max ZT	$\sigma[\mu S]$	S [μV/K]	κ_e [nW/K]	κ_p [nW/K]
Narrow Graphene	-2.05	3.48	17.6	271	0.0784	0.145
	2.08	3.51	15.5	-283	0.0676	
Narrow BN	-3.1	3.94	15.1	-255	0.0419	0.108
	3.81	3.70	22.1	247	0.110	
Narrow Si	-0.38	6.29	5.74	-339	0.0292	0.0339
	0.39	5.91	6.35	279	0.0163	
Wide C	-0.64	1.65	12.3	-241	0.0555	0.203
	0.64	1.65	12.3	241	0.0555	
Wide BN	-3.20	1.91	10.3	-259	0.0508	0.170
	2.81	1.92	10.6	271	0.0549	
Wide Si	-0.23	5.13	10.4	-296	0.0469	0.0592
	0.23	5.13	10.4	296	0.0468	

Properties of each system at 600 K at chemical potential where max ZT occurs.

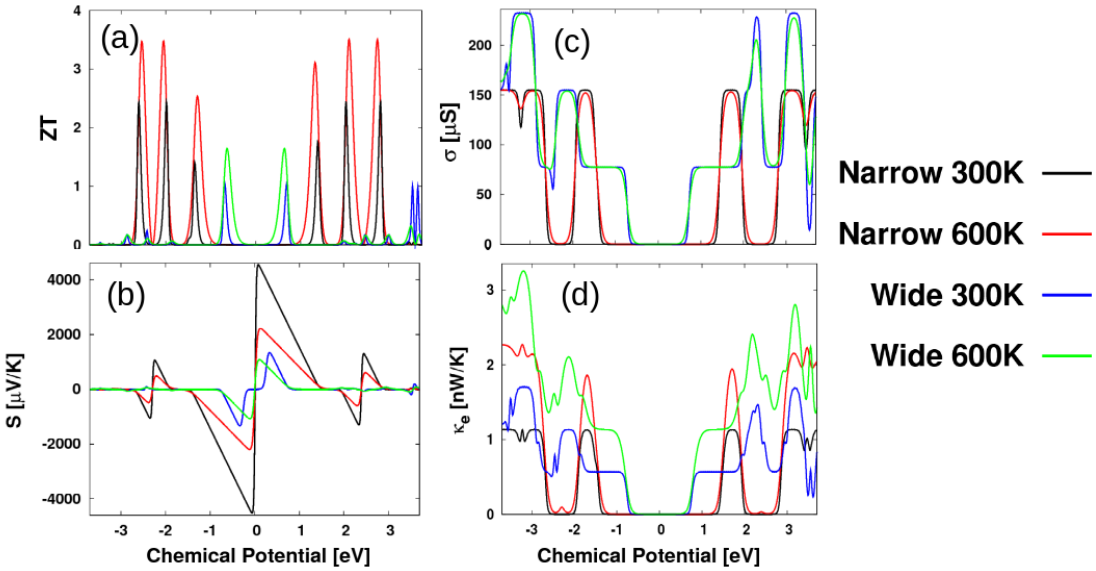

Figure 20: Thermoelectric properties of graphene nanoribbons as a function of chemical potential near the bandgap: (a) is thermoelectric figure of merit, (b) electrical conductance, (c) Seebeck coefficient, and (d) electron-contributed thermal conductance. Black and red represent narrow graphene at 300 and 600 K, respectively; blue and green are wide graphene at 300 and 600 K, again respectively.

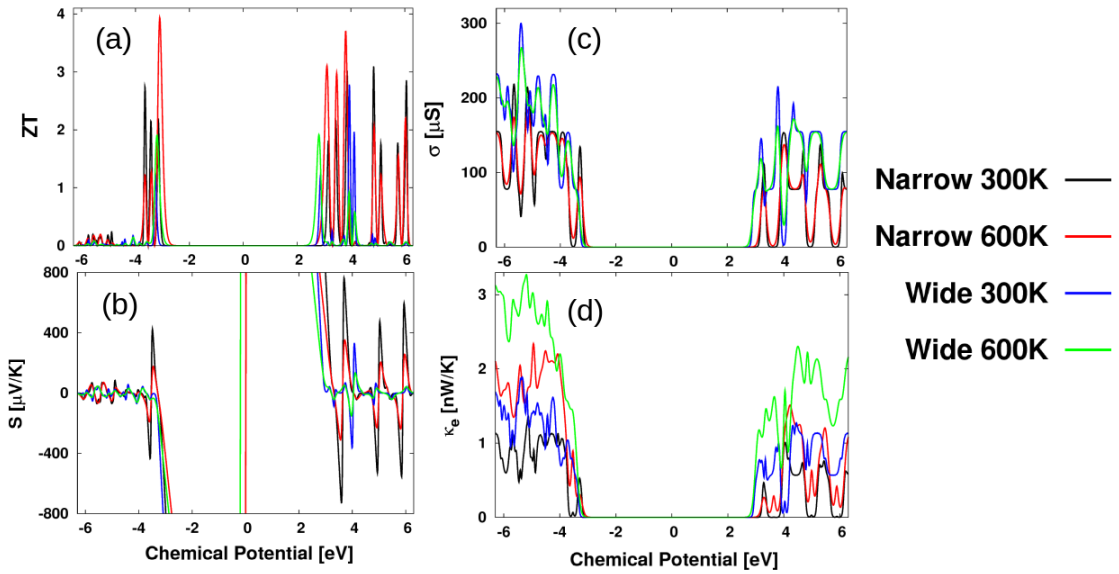

Figure 21: Thermoelectric properties of BN nanoribbons as a function of chemical potential near the bandgap: (a) is thermoelectric figure of merit, (b) electrical conductance, (c) Seebeck coefficient, and (d) electron-contributed thermal conductance. Black and red represent narrow graphene at 300 and 600 K, respectively; blue and green are wide BN at 300 and 600 K, again respectively.

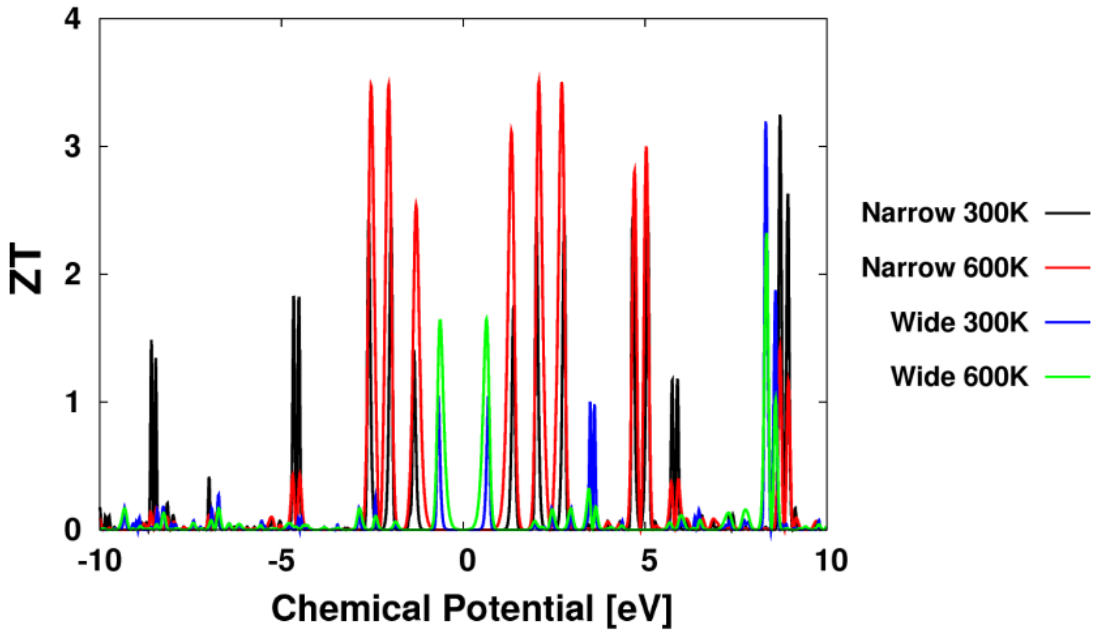

Figure 22: Thermoelectric figure of merit in narrow and wide graphene chevron nanoribbons at 300 and 600 K as a function of chemical potential, ±10 eV from the center of the bandgap of each system, which is set to 0 eV in each case.

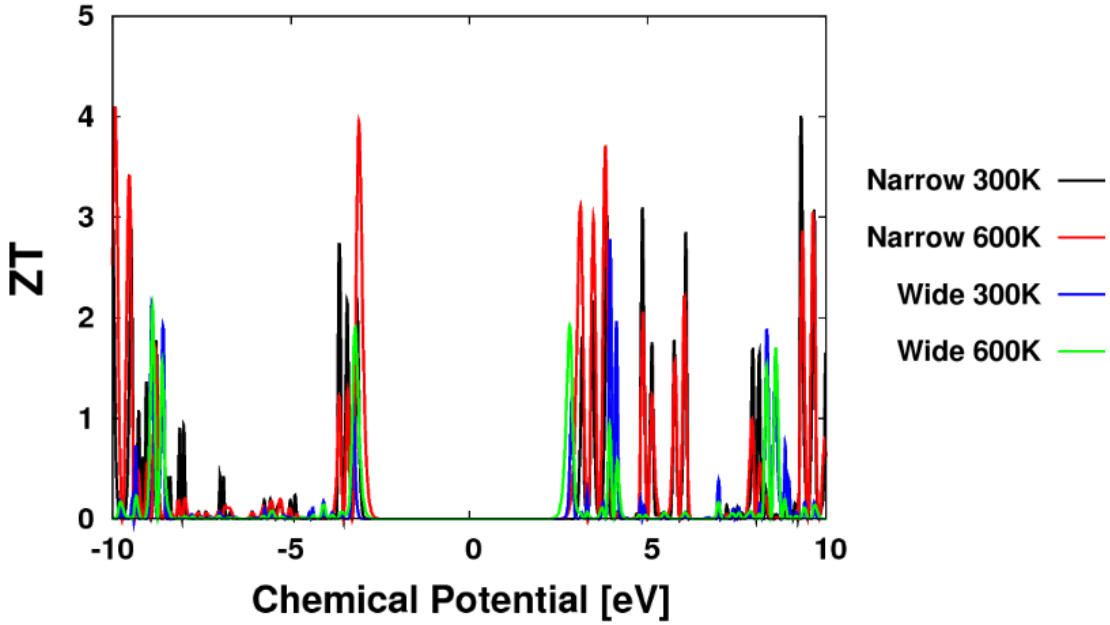

Figure 23: Thermoelectric figure of merit in narrow and wide BN chevron nanoribbons at 300 and 600 K as a function of chemical potential, ±10 eV from the center of the bandgap of each system, which is set to 0 eV in each case.

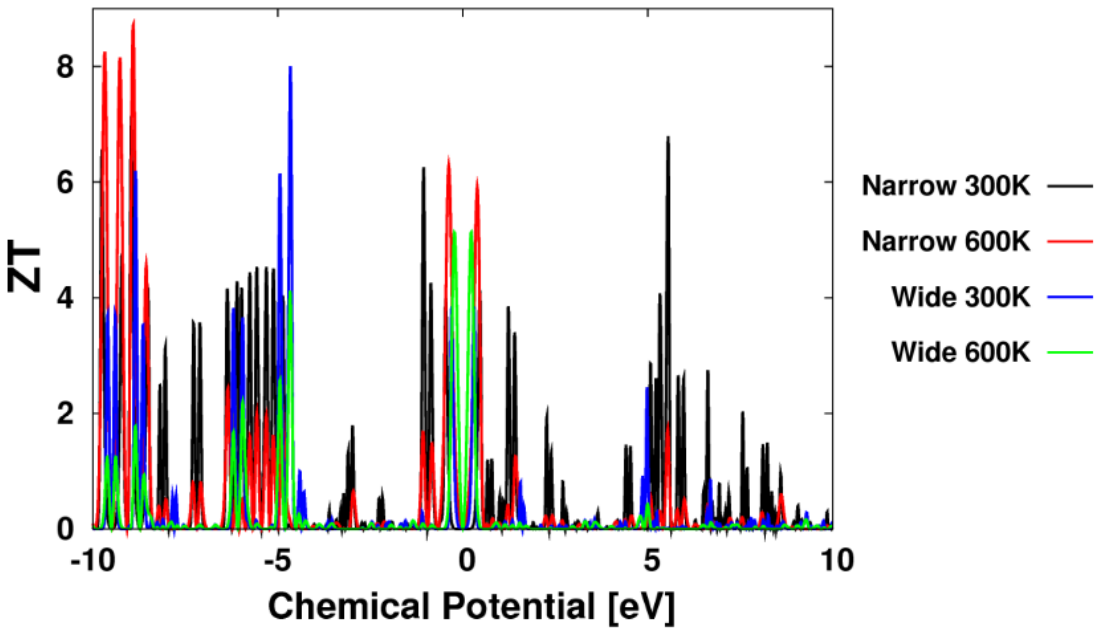

Figure 24: Thermoelectric figure of merit in narrow and wide silicene chevron nanoribbons at 300 and 600 K as a function of chemical potential, ±10 eV from the center of the bandgap of each system, which is set to 0 eV in each case.

VIII. REFERENCES

[1] F. Bonaccorso, A. Lombardo, T. Hasan, Z. Sun, L. Colombo, and A. C. Ferrari. Production and processing of graphene and 2d crystals. *Mater. Today*, 15:564, 2012.

[2] A. W. Robertson, C. S. Allen, Y. A. Wu, K. He, J. Olivier, J. Neethling, A. I. Kirkland, and J. H. Warner. Spatial control of defect creation in graphene at the nanoscale. *Nat. Commun.*, 3:1144, 2012.

[3] J. Haskins, A. Kınacı, C. Sevık, H. Sevinçli, G. Cuniberti, and T. Çağın. Control of thermal and electronic transport in defect-engineered graphene nanoribbons. *ACS Nano*, 5:3779, 2011.

[4] M. S. Hossain, F. Al-Dirini, F. M. Hossain, and E. Skafidas. High performance graphene nano-ribbon thermoelectric devices by incorporation and dimensional tuning of nanopores. *Sci. Rep.*, 5:11297, 2015.

[5] Z. W. Tan, J.-S. Wang, and C. K. Gan. First-principles study of heat transport properties of graphene nanoribbons. *Nano Lett.*, 11:214, 2011.

[6] A. A. Balandin, S. Ghosh, W. Bao, I. Calizo, D. Teweldebrhan, F. Miao, and C. N. Lau. Superior thermal conductivity of single-layer graphene. *Nano Lett.*, 8:902, 2008.

[7] S. Ghosh, I. Calizo, D. Teweldebrhan, E. P. Pokalitov, D. L. Nika, A. A. Balandin, W. Bao, F. Miao, and C. N. Lau. Extremely high thermal conductivity of graphene: Prospects for thermal management applications in nanoelectronic circuits. *Appl. Phys. Lett.*, 92:151911, 2008.

[8] E. Pop, V. Varshney, and A. K. Roy. Thermal properties of graphene: Fundamentals and applications. *MRS Bull.*, 37:1273, 2012.

[9] D. D. L. Chung. Materials for thermal conduction. *Appl. Therm. Eng.*, 21:1593, 2001.

[10] P. Goli, S. Legedza, A. Dhar, R. Salgado, J. Renteria, and A. A. Balandin. Graphene-enhanced hybrid phase change materials for thermal management of li-ion batteries. *J. Power Sources*, 113:81, 2003.

[11] J. D. Renteria, D. L. Nika, and A. A. Balandin. Graphene thermal properties: Applications in thermal management and energy storage. *Appl. Sci.*, 4:525, 2014.

[12] R. Spotnitz and J. Franklin. Abuse behavior of high-power, lithium-ion cells. *J. Power Sources*, 113:81, 2003.

[13] D. Liu, P. Yang, Z. Yuan, J. Guo, and N. Liao. The defect location effect on thermal conductivity of graphene nanoribbons based on molecular dynamics. *Phys. Lett. A*, 379:810, 2015.

[14] A. Tabarraei. Thermal conductivity of monolayer hexagonal boron nitride nanoribbons. *Comput. Mater. Sci.*, 108:66, 2015.

[15] T. Y. Ng, J. Yeo, and Z. Liu. Molecular dynamics simulation of the thermal conductivity of shorts strips of graphene and silicene: a comparative study. *Int. J. Mech. Mater. Des.*, 9:105, 2013.

[16] K. Zberecko, R. Swirkowicz, and J. Barnas. Boron nitride zigzag nanoribbons: optimal thermoelectric systems. *Phys. Chem. Chem. Phys.*, 17:22448, 2015.

[17] K. Yang, S. Cahangirov, A. Cantanero, A. Rubio, and R. D'Agosta. Thermoelectric properties of atomically thin silicene and germanene nanostructures. *Phys. Rev. B*, 89:125403, 2014.

[18] W. Zhao, Z. X. Guo, Y. Zhang, J. W. Ding, and X. J. Zheng. Enhanced thermoelectric performance of defected silicene nanoribbons. *Solid State Commun.*, 227:1, 2016.

[19] D. L. Nika, E. P. Pokatilov, A. S. Askerov, and A. A. Balandin. Phonon thermal conduction in graphene: Role of umklapp and edge roughness scattering. *Phys. Rev. B*, 79:155413, 2009.

[20] D. L. Nika, A. S. Askerov, and A. A. Balandin. Anomalous size dependence of the thermal conductivity of graphene ribbons. *Nano Lett.*, 12:3238, 2012.

[21] I. Jo, M. T. Pettes, J. Kim, K. Watanabe, T. Taniguchi, Z. Yao, and L. Shi. Thermal conductivity and phonon transport in suspended few-layer hexagonal boron nitride. *Nano Lett.*, 13:550, 2013.

[22] D. M. Rowe. Applications of nuclear-powered thermoelectric generators in space. *Appl. Energy*, 4:241, 1991.

[23] H. Alam and S. Ramakrishna. A review on the enhancement of figure of merit from bulk to nano-thermoelectric materials. *Nano Energy*, 2:190, 2013.

[24] G. Casati, C. Meja-Monasterio, and T. Prosen. Increasing thermoelectric efficiency: A dynamical systems approach. *Phys. Rev. Lett.*, 101:016601, 2008.

[25] B. Poudel, Q. Hao, Y. Ma, Y. Lan, A. Minnich, B. Yu, X. Yan, D. Wang, A. Muto, D. Vashaee, X. Chen, J. Liu, M. S. Dresselhaus, G. Chen, and Z. Ren. High-thermoelectric performance of nanostructured bismuth antimony telluride bulk alloys. *Science*, 320:634, 2008.

[26] A. Balandin and K. L. Wang. Effect of phonon confinement on the thermoelectric figure of merit of quantum wells. *J. Appl. Phys.*, 84:6149, 1998.

[27] L. D. Hicks and M. S. Dresselhaus. Effect of quantum-well structures on the thermoelectric figure of merit. *Phys. Rev. B*, 47:12727, 1993.

[28] R. Venkatasubramanian, E. Siivola, T. Colpitts, and B. O'Quinn. Thin-film thermoelectric devices with high room-temperature figures of merit. *Nature*, 413:597, 2001.

[29] H. J. Ryu, Z. Aksamija, D. M. Paskiewicz, S. A. Scott, M. G. Lagally, I. Knezevic, and M. A. Eriksson. Quantitative determination of contributions to the thermoelectric power factor in Si nanostructures. *Phys. Rev. Lett.*, 105:256601, 2010.

[30] A. I. Hochbaum, R. Chen, R. D. Delgado, W. Liang, E. C. Garnett, M. Najarian, A. Majumdar, and P. Yang. Enhanced thermoelectric performance of rough silicon nanowires. *Nature*, 451:163, 2008.

[31] X. Gu and R. Yang. First-principles prediction of phononic thermal conductivity of silicene: A comparison with graphene. *J. Appl. Phys.*, 117:025102, 2012.

[32] Y. Han, J. Dong, G. Qin, and M. Hu. Phonon transport in the ground state of two-dimensional silicon and germanium. *RSC Adv.*, 6:69956, 2016.

[33] L. Liang and V. Meunier. Electronic and thermoelectric properties of assembled graphene nanoribbons with elastic strain and structural dislocation. *Appl. Phys. Lett.*, 102:143101, 2013.

[34] V. H. Nguyen, M. C. Nguyen, H.-V. Nguyen, J. Saint-Martin, and P. Dollfus. Enhanced thermoelectric figure of merit in vertical graphene junctions. *Appl. Phys. Lett.*, 105:133105, 2014.

[35] V.-T. Tran, J. Saint-Martin, and P. Dollfus. High thermoelectric performance in graphene nanoribbons by graphene/BN interface engineering. *Nanotechnology*, 26:495202, 2015.

[36] S. V. Muley and N. M. Ravindra. Thermoelectric properties of pristine and doped graphene nanosheets and graphene nanoribbons: Part ii. *J. Min. Met. Mat. S.*, 68:1660, 2016.

[37] X. Ni, G. Liang, J.-S. Wang, and B. Li. Disorder enhances thermoelectric figure of merit in armchair graphane nanoribbons. *Appl. Phys. Lett.*, 95:192114, 2009.

[38] H. Sevinçli, C. Sevik, T. Çağın, and G. Cuniberti. A bottom-up route to enhance thermoelectric figures of merit in graphene nanoribbons. *Sci. Rep.*, 3:1228, 2013.

[39] H. Sadeghi, S. Sangtarash, and C. J. Lambert. Enhancing the thermoelectric figure of merit in engineered graphene nanoribbons. *Beilstein J. Nanotechnol.*, 6:1176, 2015.

[40] L. Liang and V. Meunier. Enhanced thermoelectric performance of graphene nanoribbons. *Appl. Phys. Lett.*, 100:093104, 2012.

[41] Z.-X. Xie, L.-M. Tang, C.-N. Pan, Q. Chen, and K.-Q. Chen. Ballistic thermoelectric properties in boron nitride nanoribbons. *J. Appl. Phys.*, 114:144311, 2013.

[42] L. A. Algharagholy, Q. Al-Galiby, H. A. Marhoon, H. Sadeghi, H. M. Abduljalil, and C. J. Lambert. Tuning thermoelectric properties of graphene/boron nitride heterostructures. *Nanotechnology*, 26:475401, 2015.

[43] K. Yang, Y. Chen, R. D'Agosta, Y. Xie, J. Zhong, and A. Rubio. Enhanced thermoelectric properties in hybrid graphene/boron nitride nanoribbons. *Phys. Rev. B*, 86:045425, 2012.

[44] L. Pan, H. J. Liu, X. J. Tan, H. Y. Lv, J. Shi, X. F. Tang, and G. Zheng. Thermoelectric properties of armchair and zigzag silicene nanoribbons. *Phys. Chem. Chem. Phys.*, 14:13588–13593, 2012.

[45] H. Sadeghi, S. Sangtarash, and C. J. Lambert. Enhanced thermoelectric efficiency of porous silicene nanoribbons. *Scientific Reports*, 5:9514, 2015.

[46] X. J. Tan, H. J. Liu, Y. W. Wen, H. Y. Lv, L. Pan, J. Shi, and X. F. Tang. Thermoelectric properties of ultrasmall single-wall carbon nanotubes. *J. Phys. Chem. C*, 115:21996, 2011.

[47] X. J. Tan, H. J. Liu, J. Wei, J. Shi, X. F. Tang, and C. Uher. Thermoelectric properties of small diameter carbon nanowires. *Carbon*, 53:286, 2013.

[48] J. Cai, P. Ruffieux, R. Jaafar, M. Bieri, T. Braun, S. Blankenburg, M. Muoth, A. P. Seitsonen, M. Saleh, X. Feng, K. Müllen, and R. Fasel. Atomically precise bottom-up fabrication of graphene nanoribbons. *Nature*, 466:470–473, 2016.

[49] N. T. Cuong, M. Otani, and S. Okada. Absence of edge states near the 120 corners of zigzag graphene nanoribbons. *Phys. Rev. B*, 87:045424, 2013.

[50] D. Szczesniak, A. P. Durajski, A. Khater, and D. Ghader. Energy band gaps in graphene nanoribbons with corners. *EPL*, 114:48001, 2016.

[51] V. A. Saroka, K. G. Batrakov, V. A. Demin, and L. A. Chernozatonskii. Band gaps in jagged and straight graphene nanoribbons tunable by an external electric field. *J. Phys. Condens. Matter*, 27:145305, 2015.

[52] W. Huang, J.-S. Wang, and G. Liang. Theoretical study on thermoelectric properties of kinked graphene nanoribbons. *Phys. Rev. B*, 84:045410, 2011.

[53] J. Lan, Y. Cai, G. Zhang, J.-S. Wang, and Y.-W. Zhang. Topological symmetry-induced width dependence of thermal conductance of edge-reconstructed graphene nanoribbons. *J. Phys. D: Appl. Phys.*, 47:265303, 2014.

[54] H. Tomita and J. Nakamura. Ballistic phonon thermal conductance in graphene nanoribbons. *J. Vac. Sci. Technol. B*, 31:4, 2013.

[55] L. Zhang, S. Diao, Y. Nie, K. Yan, N. Liu, B. Dai, Q. Xie, A. Reina, J. Kong, and Z. Liu. Photocatalytic patterning and modification of graphene. *J. Am. Chem. Soc.*, 133:2706, 2011.

[56] A. Nagashima, N. Tejima, Y. Gamou, T. Kawai, and C. Oshima. Electronic dispersion relations of monolayer hexagonal boron nitride formed on the ni(111) surface. *Phys. Rev. B*, 51:4606–4613, 1995.

[57] B. Lalmi, H. Oughaddou, H. Enriquez, A. Kara, S. Vizzini, B. Ealet, and B. Aufray. Epitaxial growth of a silicene sheet. *Appl. Phys. Lett.*, 97:223109, 2010.

[58] E. Schrödinger. An undulatory theory of the mechanics of atoms and molecules. *Phys. Rev.*, 28:1049, 1926.

[59] P. Politzer and J. S. Murray. Some intrinsic features of hydroxylamines, oximes and hydroxamic acids: Integration of theory and experiment. In Z. Rappoport and J. F. Liebman, editors, *The Chemistry of Hydroxylamines, Oximes and Hydroxamic Acids*, volume 1, chapter 1. Wiley, 2009.

[60] P. Hohenberg and W. Kohn. Inhomogeneous electron gas. *Phys. Rev.*, 136:B864, 1964.

[61] W. Kohn and L. J. Sham. Self-consistent equations including exchange and correlation effects. *Phys. Rev.*, 140:A1133, 1965.

[62] Nobel focus: Chemistry by computer. *Phys. Rev. Focus*, 2:19, 1998.

[63] A. D. Becke. Density-functional exchange-energy approximation with correct asymptotic behavior. *Phys. Rev. A*, 38:3098, 1988.

[64] C. Lee, W. Yang, and R. G. Parr. Development of the colle-salvetti correlation-energy formula into a functional of the electron density. *Phys. Rev. B*, 37:785, 1988.

[65] A. D. Becke. A new mixing of hartreefock and local densityfunctional theories. *J. Chem. Phys.*, 98:1372, 1993.

[66] R. Van Noorden, B. Maher, and R. Nuzzo. The top 100 papers. `http://www.nature.com/news/the-top-100-papers-1.16224`, 2014.

[67] E. R. Brown. Physics 7310 lectures 8, 27. Wright State University Lecture, 2016.

[68] L. Liang, E. Cruz-Silva, E. C. Girão, and V. Meunier. Enhanced thermoelectric figure of merit in assembled graphene nanoribbons. *Phys. Rev. B*, 86:115438, 2012.

[69] M. J. Frisch, G. W. Trucks, H. B. Schlegel, G. E. Scuseria, M. A. Robb, J. R. Cheeseman, G. Scalmani, V. Barone, B. Mennucci, G. A. Petersson, H. Nakatsuji, M. Caricato, X. Li, H. P. Hratchian, A. F. Izmaylov, J. Bloino, G. Zheng, J. L. Sonnenberg, M. Hada, M. Ehara, K. Toyota, R. Fukuda, J. Hasegawa, M. Ishida, T. Nakajima, Y. Honda, O. Kitao, H. Nakai, T. Vreven, J. A. Montgomery, Jr., J. E. Peralta, F. Ogliaro, M. Bearpark, J. J. Heyd, E. Brothers, K. N. Kudin, V. N. Staroverov, R. Kobayashi, J. Normand, K. Raghavachari, A. Rendell, J. C. Burant, S. S. Iyengar, J. Tomasi, M. Cossi, N. Rega, J. M. Millam, M. Klene, J. E. Knox, J. B. Cross, V. Bakken, C. Adamo, J. Jaramillo, R. Gomperts, R. E. Stratmann, O. Yazyev, A. J. Austin, R. Cammi, C. Pomelli, J. W. Ochterski, R. L. Martin, K. Morokuma, V. G. Zakrzewski, G. A. Voth, P. Salvador, J. J. Dannenberg, S. Dapprich, A. D. Daniels, O. Farkas, J. B. Foresman, J. V. Ortiz, J. Cioslowski, and D. J. Fox. Gaussian 09 Revision A.02. Gaussian Inc. Wallingford CT 2009.

[70] G09 keyword: Opt. `http://www.gaussian.com/g_tech/g_ur/k_opt.htm`. Accessed: 2016-12-11.

[71] T. Wassman, A. P. Seitsonen, A. M. Saitta, M. Lazzeri, and F. Mauri. Structure, stability, edge states, and aromaticity of graphene ribbons. *Phys. Rev. Lett.*, 101:096402, 2008.

[72] A. A. Farajian, R. V. Belosludov, H. Mizuseki, and Y. Kawazoe. A general-purpose approach for calculating transport in contactmoleculecontact systems: TARABORD implementation and application to a polythiophene-based nanodevice. *Thin Solid Films*, 499:269–274, 2006.

[73] W. Zhang, T. S. Fisher, and N. Mingo. The atomistic green's function method: An efficient simulation approach for nanoscale phonon transport. *Numer. Heat Transfer B*, 51:333, 2007.

[74] J.-S. Wang, J. Wang, and J. T. Lü. Quantum thermal transport in nanostructures. *Eur. Phys. J. B*, 62:381, 2008.

[75] Z.-X. Xie, K.-Q. Chen, and W. J. Duan. Thermal transport by phonons in zigzag graphene nanoribbons with structural defects. *J. Phys. Condens. Matter*, 23:315302, 2011.

[76] A. Calzolari, T. Jayasekera, K. W. Kim, and M. B. Nardelli. Ab initio thermal transport properties of nanostructures from density functional perturbation theory. *J. Phys. Condens. Matter*, 24:492204, 2012.

[77] T. H. Osborn. *Computational Design and Characterization of Silicene Nanostructures for Electrical and Thermal Transport Applications.* PhD thesis, Wright State University, May 2014.

[78] L. G. C. Rego and G. Kirczenow. Quantized thermal conductance of dielectric quantum wires. *Phys. Rev. Lett.*, 81:232, 1998.

[79] K. Schwab, E. A. Henriksen, J. M. Worlock, and M. L. Roukes. Measurement of the quantum of thermal conductance. *Nature*, 404:974, 2000.

[80] M. Topsakal, E. Aktrk, and S. Ciraci. First-principles study of two- and one-dimensional honeycomb structures of boron nitride. *Phys. Rev. B*, 79:115442, 2009.

[81] N. Mounet and N. Marzari. Nuclear quantum effects on the thermal expansion coefficient of hexagonal boron nitride monolayer. *Phys. Rev. B*, 71:205214, 2005.

[82] F. Calvo and Y. Magnin. Nuclear quantum effects on the thermal expansion coefficient of hexagonal boron nitride monolayer. *Eur. Phys. J. B*, 89:56, 2016.

[83] T. H. Osborn and A. A. Farajian. Stability of lithiated silicene from first principles. *J. Phys. Chem C*, 116:22916, 2012.

[84] E. Valeev. Basis sets in quantum chemistry. `http://www.valeevgroup.chem.vt.edu/docs/basisset_notes.07032015.pdf`. Accessed: 2016-12-11.

[85] A. A. Farajian, R. V. Belosludov, H. Mizuseki, Y. Kawazoe, T. Hashizume, and B. I. Yakobson. Gate-induced switching and negative differential resistance in a single-molecule transistor: Emergence of fixed and shifting states with molecular length. *J. Chem. Phys.*, 127:024901, 2007.

[86] R. V. Belosludov, A. A. Farajian, H. Mizuseki, K. Miki, and Y. Kawazoe. Electronic and transport properties of bismuth nanolines for applications in molecular electronics. *Phys. Rev. B.*, 75:113411, 2007.

[87] A. Sadrzadeh, A. A. Farajian, and B. I. Yakobson. Electron transport of nanotube-based gas sensors: An ab initio study. *Appl. Phys. Lett.*, 92:022103, 2008.

[88] L. J. Wirth, T. H. Osborn, and A. A. Farajian. Resilience of thermal conductance in defected graphene, silicene, and boron nitride nanoribbons. *Appl. Phys. Lett.*, 109:173102, 2016.

[89] H. M. Pastawski. Classical and quantum transport from generalized Landauer-Büttiker equations. *Phys. Rev. B*, 44:6329–6339, 1991.

[90] S. Datta. *Electronic Transport in Mesoscopic Systems*. Cambridge University Press, Cambridge, U.K., 1995.

[91] M. B. Nardelli. Electronic transport in extended systems: Application to carbon nanotubes. *Phys. Rev. B*, 60:7828, 1999.

[92] U. Sivan and Y. Imry. Multichannel landauer formula for thermoelectric transport with application to thermopower near the mobility edge. *Phys. Rev. B*, 33:551, 1986.

[93] K. Esfarjani, M. Zebarjadi, and Y. Kawazoe. Thermoelectric properties of a nanocontact made of two-capped single-wall carbon nanotubes calculated within the tight-binding approximation. *Phys. Rev. B*, 73:085406, 2006.

[94] G09 keyword: SCF. `http://www.gaussian.com/g_tech/g_ur/k_scf.htm`. Accessed: 2016-12-04.

[95] G09 keyword: Integral. `http://www.gaussian.com/g_tech/g_ur/k_integral.htm`. Accessed: 2016-12-04.

[96] G09 Rev. E.01 release notes. `http://www.gaussian.com/g_tech/rel_notes.pdf`. Accessed: 2016-12-04.

[97] M. J. Frisch, G. W. Trucks, H. B. Schlegel, G. E. Scuseria, M. A. Robb, J. R. Cheeseman, G. Scalmani, V. Barone, B. Mennucci, G. A. Petersson, H. Nakatsuji, M. Caricato, X. Li, H. P. Hratchian, A. F. Izmaylov, J. Bloino, G. Zheng, J. L. Sonnenberg, M. Hada, M. Ehara, K. Toyota, R. Fukuda, J. Hasegawa, M. Ishida, T. Nakajima, Y. Honda, O. Kitao, H. Nakai, T. Vreven, J. A. Montgomery, Jr., J. E. Peralta, F. Ogliaro, M. Bearpark, J. J. Heyd, E. Brothers, K. N. Kudin, V. N. Staroverov, R. Kobayashi, J. Normand, K. Raghavachari, A. Rendell, J. C. Burant,

S. S. Iyengar, J. Tomasi, M. Cossi, N. Rega, J. M. Millam, M. Klene, J. E. Knox, J. B. Cross, V. Bakken, C. Adamo, J. Jaramillo, R. Gomperts, R. E. Stratmann, O. Yazyev, A. J. Austin, R. Cammi, C. Pomelli, J. W. Ochterski, R. L. Martin, K. Morokuma, V. G. Zakrzewski, G. A. Voth, P. Salvador, J. J. Dannenberg, S. Dapprich, A. D. Daniels, O. Farkas, J. B. Foresman, J. V. Ortiz, J. Cioslowski, and D. J. Fox. Gaussian 09 Revision E.01. Gaussian Inc. Wallingford CT 2009.

[98] Ohio Supercomputer Center. Ohio supercomputer center. `http://osc.edu/ark:/19495/f5s1ph73`, 1987.

[99] E. Cinquanta, E. Scalise, D. Chiappe, C. Grazianetti, B. v. d. Broek, M. Houssa, M. Fanciulli, and A. Molle. Getting through the nature of silicene: An sp^2sp^3 two-dimensional silicon nanosheet. *J. Phys. Chem. C*, 117:16719, 2013.

[100] J.-W. Jiang, B.-S. Wang, and J.-S. Wang. First principle study of the thermal conductance in graphene nanoribbon with vacancy and substitutional silicon defects. *Appl. Phys. Lett.*, 98:113114, 2011.

[101] K. Yang, Y. Chen, Y. Xie, X. L. Wie, T. Ouyang, and J. Zhong. Effect of triangle vacancy on thermal transport in boron nitride nanoribbons. *Solid State Commun.*, 151:460, 2011.

[102] T. Ouyang, Y. Chen, Y. Xie, K. Yang, Z. Bao, and J. Zhong. Thermal transport in hexagonal boron nitride nanoribbons. *Nanotechnology*, 21:245701, 2010.

[103] B. Cao, W. Yao, and Z. Ye. Networked nanoconstrictions: An effective route to tuning the thermal transport properties of graphene. *Carbon*, 96:711, 2016.

[104] F. Hao, D. Fang, and Z. Xu. Mechanical and thermal transport properties of graphene with defects. *Appl. Phys. Lett.*, 99:041901, 2011.

[105] H. Zhang, G. Lee, and K. Cho. Thermal transport in graphene and effects of vacancy defects. *Phys. Rev. B*, 79:115442, 2009.

[106] T. Feng, X. Ruan, Z. Ye, and B. Cao. Spectral phonon mean free path and thermal conductivity accumulation in defected graphene: The effects of defect type and concentration. *Phys. Rev. B*, 91:224301, 2015.

[107] J. Lan, J.-S. Wang, C. K. Gan, and S. K. Chin. Edge effects on quantum thermal transport in graphene nanoribbons: Tight-binding calculations. *Phys. Rev. B*, 79:115401, 2009.

[108] H. Sevinçli and G. Cuniberti. Enhanced thermoelectric figure of merit in edge-disordered zigzag graphene nanoribbons. *Phys. Rev. B*, 81:113401, 2010.

[109] H. Karamitaheri, M. Pourfath, H. Kosina, and N. Neophytou. Low-dimensional phonon transport effects in ultranarrow disordered graphene nanoribbons. *Phys. Rev. B*, 91:165410, 2015.

[110] G. Xie and Y. Shen. Size and edge roughness dependence of thermal conductivity for vacancy-defective graphene ribbons. *Phys. Chem. Chem. Phys.*, 17:8822, 2015.

[111] C. Wang, T. Ouyang, Y. Chen, and J. Zhong. Enhancement of thermoelectric properties of gamma-graphyne nanoribbons with edge modulation. *Eur. Phys. J. B*, 88:130, 2015.

[112] T. H. Osborn and A. A. Farajian. Silicene nanoribbons as carbon monoxide nanosensors with molecular resolution. *Nano Research*, 7:945, 2014.

[113] Z. Ni, Q. Liu, K. Tang, J. Zheng, J. Zhou, R. Qin, Z. Gao, D. Yu, and J. Lu. Tunable bandgap in silicene and germanene. *Nano. Lett.*, 466:113, 2012.

[114] N. D. Drummond, V. Zlyomi, and V. I. Fal'ko. Electrically tunable band gap in silicene. *Phys. Rev. B*, 85:075423, 2012.

[115] B. Liu, J. A. Baimova, C. D. Reddy, S. V. Dmitriev, W. K. Law, and X. Q. Feng. Interface thermal conductance and rectification in hybrid graphene/silicene monolayer. *Carbon*, 79:236, 2014.